



LAWRENCE  
LIVERMORE  
NATIONAL  
LABORATORY

# High Order Curvilinear Finite Elements for Lagrangian Hydrodynamics

V. A. Dobrev, T. V. Kolev, R. N. Rieben

November 28, 2011

SIAM Journal of Scientific Computing

## **Disclaimer**

---

This document was prepared as an account of work sponsored by an agency of the United States government. Neither the United States government nor Lawrence Livermore National Security, LLC, nor any of their employees makes any warranty, expressed or implied, or assumes any legal liability or responsibility for the accuracy, completeness, or usefulness of any information, apparatus, product, or process disclosed, or represents that its use would not infringe privately owned rights. Reference herein to any specific commercial product, process, or service by trade name, trademark, manufacturer, or otherwise does not necessarily constitute or imply its endorsement, recommendation, or favoring by the United States government or Lawrence Livermore National Security, LLC. The views and opinions of authors expressed herein do not necessarily state or reflect those of the United States government or Lawrence Livermore National Security, LLC, and shall not be used for advertising or product endorsement purposes.

# HIGH-ORDER CURVILINEAR FINITE ELEMENT METHODS FOR LAGRANGIAN HYDRODYNAMICS \*

V. A. DOBREV, <sup>†</sup>, TZ. V. KOLEV <sup>‡</sup>, AND R. N. RIEBEN <sup>§</sup>

## Abstract.

We derive a general finite element approach for solving the Euler equations of compressible hydrodynamics in a moving Lagrangian frame. We discretize the kinematic variables of position and velocity using a continuous high-order basis function expansion of arbitrary polynomial degree which is obtained via a corresponding high-order parametric mapping from a standard reference element. This enables the use of curvilinear zone geometry, higher-order approximations for fields within a zone and a pointwise definition of mass conservation which we refer to as strong mass conservation. We discretize the internal energy using a piecewise discontinuous high-order basis function expansion which is also of arbitrary polynomial degree. This facilitates multi-material hydrodynamics by treating material properties, such as equations of state and constitutive models, as piecewise discontinuous functions which vary within a zone. To satisfy the Rankine-Hugoniot jump conditions at a shock boundary and generate the appropriate entropy, we introduce a general tensor artificial viscosity which takes advantage of the high-order kinematic and thermodynamic information available in each zone. Finally, we apply a generic high-order time discretization process to the semi-discrete equations to develop the fully discrete conservation laws. Our method can be viewed as the high-order generalization of the so called staggered-grid hydrodynamics (SGH) approach and we show that under specific low order assumptions, we exactly recover the classical SGH method. Our method is valid for both 2D and 3D meshes with quadrilateral/hexahedral and triangular/tetrahedral zones. We present an extensive series of verification test problems designed to stress important aspects of Lagrangian hydrodynamics and to demonstrate several practical advantages to using high-order finite elements in this context, including: the ability to more accurately capture geometrical features of a flow region using curvilinear zones, significant improvements in symmetry preservation for symmetric flows, elimination of the need for ad-hoc hourglass filters, sharper resolution of a shock front for a given mesh resolution including the ability to represent a shock within a single zone and a substantial reduction in mesh imprinting for shock wave propagation not aligned with the computational mesh.

**Key words.** Hydrodynamics; Compressible flow; Hyperbolic partial differential equations; Lagrangian methods; Finite element methods; Variational methods; High-order methods; Curvilinear meshes

**AMS subject classifications.** 65M60, 76N15, 76L05

**1. Introduction and Motivation.** Our goal is to solve the Euler equations of compressible hydrodynamics for the purposes of modeling complex, multi-material, high speed flow and shock wave propagation over general unstructured 2D and 3D computational domains. Numerical methods for solving such equations can be classified according to two classical cases: the Eulerian and the Lagrangian descriptions. In the Eulerian case, numerical methods are defined on a fixed, typically Cartesian, computational mesh through which the fluid moves. In contrast, Lagrangian methods are characterized by a computational mesh that moves with the fluid velocity. The advantages, disadvantages and applications of each approach are well documented (see for example [1]). In this paper, we are concerned exclusively with Lagrangian methods.

---

\*This work performed under the auspices of the U.S. Department of Energy by Lawrence Livermore National Laboratory under Contract DE-AC52-07NA27344, LLNL-JRNL-XXXXXX

<sup>†</sup>Center for Applied Scientific Computing, Lawrence Livermore National Laboratory, dobrev1@llnl.gov,

<sup>‡</sup>Center for Applied Scientific Computing, Lawrence Livermore National Laboratory, tzanio@llnl.gov

<sup>§</sup>Weapons and Complex Integration, B-Division, Lawrence Livermore National Laboratory, rieben1@llnl.gov

Historically, Lagrangian methods have been achieved using one of two major approaches. The first, known as staggered grid hydrodynamics (SGH), employs a spatial discretization where the thermodynamic variables density, pressure and internal energy are approximated as piecewise constant values defined on zone centers and kinematic variables such as velocity and accelerations are defined on the mesh nodes (vertices); cf. [2, 3, 4]. Artificial viscosity, as originally proposed by [5], is used to generate entropy across shock boundaries while still satisfying the Rankine-Hugoniot jump conditions at an appropriate distance away from the shock (typically a few zones). The second major approach, known as cell-centered hydrodynamics (CCH), treats all hydrodynamic variables as zone (or cell) averaged quantities and uses approximate Riemann solvers (in the spirit of Godunov methods) to determine velocities at mesh vertices; cf [6, 7, 8]. This process naturally introduces a sufficient level of dissipation at shock boundaries. We note that work has been done which attempts to bridge the conceptual gap between these approaches and identifies many similarities between them [9, 10].

For each of these approaches, the node based kinematic variables are required to be continuous in order to have a well defined field with which to move the mesh at each discrete time step; whereas the thermodynamic variables are discontinuous. This is usually referred to as a "single fluid, multiple material" approximation of the general hydrodynamics equations. The distinction of continuous vs. discontinuous thermodynamic variables is trivial for the case of constant zone averaged values, but becomes important when we consider the more general case of higher order bases for thermodynamic fields. There is physical motivation for treating these variables in a discontinuous manner since the equation of state of a material is a local property and discontinuous at material interfaces (contact discontinuities). The preservation of material interfaces is one of the attractive features of a Lagrangian method.

Typically, SGH and CCH methods employ finite difference or finite volume techniques to compute spatial gradients which are required for calculating forces. For example, in the case of SGH, the forces acting on a given mesh node due to the gradient of the scalar pressure field are computed using the pressure values and mesh coordinates of the zones which share that node. Since the mesh is an evolving quantity throughout the duration of a Lagrangian computation, its quality changes from time step to time step and therefore influences the solution accuracy via the strong dependence on local mesh spacing and quality for finite difference / finite volume gradient computations. This strong dependence on local mesh quality leads to the so called "mesh imprinting" phenomenon where a Lagrangian calculation can prematurely terminate due to mesh tangling or an overly restrictive Courant limited time step. Furthermore, this mesh based error feeds back into the computation in a non-linear fashion and can therefore be amplified over time leading to non-physical results such as symmetry breaking and spurious grid vorticity [11]. In addition to mesh imprinting, SGH Lagrangian calculations have long suffered from the so called "hour-glass mode" instabilities which are caused by the inability of a numerical method to resolve the gradient of the highest frequency spatial mode of a given computational grid (the so-called "checkerboard" pressure mode). If left unchecked, such modes can grow indefinitely in a time dependent problem leading to spurious grid distortion. To address this instability, it is often necessary to introduce artificial forces in the momentum equation which are designed to resist (or filter out) the offending modes [4].

The arbitrary Lagrangian-Eulerian (ALE) technique was developed largely to



overcome many of these issues [12, 13, 14, 15]. In a typical ALE implementation, the mesh is evolved in a Lagrangian manner for some number of time steps, until the so called re-meshing phase at which point the computational mesh is adjusted according to some prescribed quality metrics followed by the remap phase where the solution variables are conservatively and monotonically remapped onto the new mesh. The ALE technique is a very mature methodology and is the basis for many large scale, massively parallel simulation codes; the details of ALE will not be considered in this paper. At the core of every ALE method is the Lagrange step, where the numerical solution is obtained by solving on a computational mesh which has been moved with the fluid. It is important to emphasize that despite its many advantages in maintaining mesh quality and general robustness, ALE will not solve the underlying errors in symmetry, hourglass instabilities and energy conservation that are generated by the Lagrange step.

There has been much work in developing improvements to both the SGH and CCH approaches. The so called "compatible hydro" approach of [16, 17, 18] was developed to overcome several of the long standing deficiencies of Lagrangian methods, including the inability of many methods to conserve total numerical energy algebraically. In the compatible method, the notion of sub-zonal "corner masses" and corresponding "corner forces" are introduced which are used to compute work terms for updating the internal energy in a manner which conserves total energy algebraically. Furthermore, the corner masses are used to infer sub-zonal pressure changes which are then used to compute internal zone forces designed to resist hourglass mode deformations, zone "collapse" and in general, to improve the robustness of Lagrangian computations. Taking a different approach to improving the quality of Lagrangian methods, several researchers have advocated the use of improved artificial viscosities for SGH formulations such as the edge and tensor artificial viscosity formulations of [19, 20, 21, 22]. Similar work has been done for the case of CCH Lagrangian methods by improving the way in which nodal velocities are obtained as in [10]

Recent work has been made connecting the traditional SGH methods to finite element methods (FEM). In [23, 24] the authors introduce the use of stabilized  $Q1/P0$  elements for multi-scale Lagrangian hydrodynamics where they make use of many techniques from finite element theory, such as parametric element mappings, mass and stiffness matrices, and mass lumping to formulate their methods. Furthermore, a connection between the compatible hydro method and traditional finite element methods is described in [25].

We consider a generalized FEM treatment (cf. [26]) that includes the case of higher order basis functions obtained via a high-order mapping from a reference element. We treat the equations of momentum and energy conservation in a variational manner and employ a Galerkin finite element discretization process to reduce the continuum equations to a set of semi-discrete algebraic equations. We then apply a generalized high-order time stepping procedure to the semi-discrete equations resulting in a method that is high-order accurate in both space and time. Such approaches have been successfully used in other computational physics applications including electromagnetics [27, 28, 29], incompressible flow [30] and magnetohydrodynamics [31]. In this paper we restrict ourselves to 2D/3D Cartesian geometry, but the finite element framework can be naturally extended to axisymmetric problems, as will be discussed in a different paper.

Our method is built around the notion of general high-order polynomial basis function representations for the various Lagrangian state variables. This leads to

many novel features including: curvilinear zone geometries (also explored in [32, 27]), the notion of strong mass conservation which is a point-wise generalization of zonal mass conservation, high-order continuous velocities (e.g. biquadratic, bicubic, biquartic ...), high-order discontinuous thermodynamic variables, the generalization of the "corner force" concept to high-order cases which leads to total discrete energy conservation by construction, a high-order treatment of the tensor artificial viscosity, novel variants of the artificial viscosity coefficient to account for curvilinear zone geometry and the generalization of the sub-zonal pressure method of [18] by treating the equations of state as functions which vary inside of a zone. Furthermore, we show that our general method exactly reduces to classical SGH under specific low order assumptions.

We consider an extensive set of test problems designed to exercise various aspects of Lagrangian hydrodynamics including 1D shock / rarefaction / contact discontinuity propagation, preservation of adiabats for smooth flow, shock wave propagation over general / distorted meshes, symmetry preservation for radial and spherical flows on general meshes, spurious vorticity / enstrophy generation for smooth nearly incompressible flows and complex shock interactions on unstructured grids. For each case we demonstrate the advantages that our generalized high-order approach can provide.

The remainder of this paper is organized as follows: In Section 2 we review the continuum equations of Lagrangian hydrodynamics. In Section 3 we consider a generic finite dimensional variational formulation of the Euler equations in a Lagrangian frame. In Section 4 we present a finite element numerical algorithm based on the general semi-discrete Lagrangian discretization method which uses high order finite element spaces defined on curvilinear zone geometries obtained through a high order mapping from a reference element. In Section 5 we prove equivalence of the resulting general finite element formulas to some classical SGH methods under simplifying, low order approximations. In Section 6 we discuss the details of artificial viscosity for the general high-order methods and introduce several novel concepts for treating the artificial viscosity coefficient in this context. In Section 7 we apply a generic time discretization process to the semi-discrete equations and develop the fully discrete conservations laws. Finally, in Section 8 we present an extensive series of verification test problems solved using the newly develop method and demonstrate its practical advantages over a wide scope of problem types.

**2. Conservation Laws of Lagrangian Hydrodynamics.** Consider a continuous medium,  $\Omega(t)$ , e.g. a fluid or elastic body which is deforming in time. We think of the medium as composed of a continuum number of particles,  $\{x(t)\}$ , which occupy different points in space for different values of  $t$ . The initial configuration at time  $t = t_0$  will be denoted by  $\tilde{\Omega} \equiv \Omega(t_0)$  and its particles by  $\{\tilde{x}\}$ . In the Lagrangian description of motion, the particle position  $x$  is expressed as a function of the initial position  $\tilde{x}$  and time:

$$x = x(\tilde{x}, t) = \tilde{\Phi}(\tilde{x}, t), \quad \tilde{x} \in \tilde{\Omega}, \quad t \geq t_0. \quad (2.1)$$

This description corresponds to an observer moving with the medium and is characterized by the use of the material derivative

$$\frac{d\alpha}{dt}(x, t) = \frac{d}{dt}[\alpha(x(\tilde{x}, t), t)], \quad \text{or} \quad \frac{d\alpha}{dt} = \frac{\partial \alpha}{\partial t} + v \cdot \nabla \alpha. \quad (2.2)$$

Here  $\alpha = \alpha(x, t)$  is any quantity (scalar, vector, etc.) associated with the fluid, while  $v$  is the particle velocity, i.e. the rate of change of the particle position relative to an

outside observer or Eulerian reference frame:

$$v(x, t) = \frac{dx}{dt} \equiv \frac{\partial \tilde{\Phi}(\tilde{x}, t)}{\partial t}. \quad (2.3)$$

Note that in (2.2) and the rest of the paper we use the derivative and contraction operators according to general tensor rules, so e.g.  $(v \cdot \nabla v)_j = \sum_i v_i (\partial_i v_j)$ .

The conservation laws of Lagrangian hydrodynamics are a direct consequence of the following result, known as the *Reynolds transport theorem*, see e.g. [33, 34], which describes the rate of change of integrated quantities (like mass, momentum and energy):

$$\frac{d}{dt} \int_{U(t)} \alpha = \int_{U(t)} \frac{d\alpha}{dt} + \alpha \nabla \cdot v. \quad (2.4)$$

Here  $U(t) = \tilde{\Phi}(\tilde{U}, t)$  is an arbitrary control volume (a set of particles), which deforms in time starting from an original configuration  $\tilde{U} \subset \tilde{\Omega}$ .

The Reynolds transport theorem can be derived using change of variables and the identity

$$\frac{d|\tilde{J}|}{dt} = |\tilde{J}| \nabla \cdot v, \quad (2.5)$$

where  $\tilde{J} = \nabla_{\tilde{x}} x = \nabla_{\tilde{x}} \tilde{\Phi}$  is the Jacobian of the Lagrangian transformation (2.1) and  $|\tilde{J}|$  is its determinant.

Setting  $\alpha = 1$  in (2.4) gives the so-called geometric conservation law (GCL)

$$\frac{d|U(t)|}{dt} = \int_{U(t)} \nabla \cdot v, \quad (2.6)$$

where  $|U(t)|$  denotes the volume of  $U(t)$ .

**2.1. Mass conservation.** Let  $\rho$  be the density (mass per volume) of the fluid. A fundamental postulate of Lagrangian hydrodynamics is that the mass in any volume  $U(t)$  does not change in time:

$$\frac{d}{dt} \int_{U(t)} \rho = 0. \quad (2.7)$$

Using the Reynolds transport theorem (2.4), this becomes

$$\int_{U(t)} \frac{d\rho}{dt} = - \int_{U(t)} \rho \nabla \cdot v, \quad (2.8)$$

which assuming regularity of the integrands, implies the point-wise equality

$$\frac{1}{\rho} \frac{d\rho}{dt} = -\nabla \cdot v. \quad (2.9)$$

Equivalently, the mass conservation law can also be expressed as

$$\frac{d}{dt}(\rho|\tilde{J}|) = 0, \quad \text{or} \quad \rho(x, t)|\tilde{J}(\tilde{x}, t)| = \rho(\tilde{x}, t_0), \quad (2.10)$$

where  $x = \tilde{\Phi}(\tilde{x}, t)$  and arbitrary  $\tilde{x} \in \tilde{\Omega}$  and  $t$ . When used directly for discretization, we refer to the above identity as the *strong mass conservation* principle, to emphasize that it is equivalent with exact mass conservation for any Lagrangian volume.

Note that the Reynolds transport theorem (2.4) and (2.9) imply

$$\frac{d}{dt} \int_{U(t)} \rho \alpha = \int_{U(t)} \rho \frac{d\alpha}{dt}, \quad (2.11)$$

which can also be derived directly.

**2.2. Momentum Conservation.** Let  $\sigma$  be the deformation stress tensor. In the absence of external body forces, the conservation of momentum reads

$$\frac{d}{dt} \int_{U(t)} \rho v = \int_{\partial U(t)} n \cdot \sigma, \quad (2.12)$$

where  $\partial U(t)$  denotes the boundary of the control volume  $U(t)$ . Using (2.11) and the divergence theorem we get

$$\int_{U(t)} \rho \frac{dv}{dt} = \int_{U(t)} \nabla \cdot \sigma, \quad (2.13)$$

which further implies the point-wise equality

$$\rho \frac{dv}{dt} = \nabla \cdot \sigma. \quad (2.14)$$

**2.3. Energy Conservation.** Let  $e$  denote the internal energy per unit mass. Then, the total internal energy in  $U(t)$  is

$$IE(t) = \int_{U(t)} \rho e. \quad (2.15)$$

Furthermore, we define the kinetic energy

$$KE(t) = \frac{1}{2} \int_{U(t)} \rho |v|^2, \quad (2.16)$$

and the total energy

$$E(t) = KE(t) + IE(t). \quad (2.17)$$

In the absence of a heat flux, the conservation of total energy can be expressed as

$$\frac{d}{dt} \int_{U(t)} \rho \left( e + \frac{1}{2} |v|^2 \right) = \int_{\partial U(t)} n \cdot \sigma \cdot v. \quad (2.18)$$

Simplifying, using (2.11), the point-wise momentum conservation (2.14), along with the fact that  $\nabla \cdot (\sigma \cdot v) = (\nabla \cdot \sigma) \cdot v + \sigma : \nabla v$ , we get

$$\int_{U(t)} \rho \frac{de}{dt} = \int_{U(t)} \sigma : \nabla v, \quad (2.19)$$

and therefore, for regular integrands

$$\rho \frac{de}{dt} = \sigma : \nabla v. \quad (2.20)$$

**2.4. Equation of State.** In gas dynamics, the stress tensor is isotropic and has the form  $\sigma = -pI$ . Here  $p$  is the thermodynamic pressure, which can be expressed as a function of the density and the internal energy through a constitutive relation  $p = EOS(\rho, e)$ . This function, known as the equation of state, is determined by experiments, and though analytical forms are available in simple cases, in practice it is typically given as tabulated data. In the (simplest) case of a polytropic ideal gas with a constant adiabatic index  $\gamma > 1$ , the EOS has the form

$$p = (\gamma - 1)\rho e. \quad (2.21)$$

**2.4.1. The Euler Equations in Differential Form.** Combining (2.14), (2.9), (2.20) and (2.21) we can write down the system of Euler equations of gas dynamics in a Lagrangian reference frame [35]:

$$\text{Momentum Conservation: } \rho \frac{dv}{dt} = \nabla \cdot \sigma, \quad (2.22)$$

$$\text{Mass Conservation: } \frac{1}{\rho} \frac{d\rho}{dt} = -\nabla \cdot v, \quad (2.23)$$

$$\text{Energy Conservation: } \rho \frac{de}{dt} = \sigma : \nabla v, \quad (2.24)$$

$$\text{Equation of Motion: } \frac{dx}{dt} = v, \quad (2.25)$$

$$\text{Equation of State: } \sigma = -EOS(\rho, e)I. \quad (2.26)$$

We use a general stress tensor  $\sigma$  in the above formulation in order to accommodate the inclusion of anisotropic tensor artificial viscosity stresses. Specifically, in Section 6 we will replace (2.26) with  $\sigma = -pI + \sigma_a$ , where  $\sigma_a$  will generally depend on all other variables.

**3. Semi-discrete Lagrangian Discretization.** In this section we consider generic finite dimensional variational formulation of the Euler equations in a Lagrangian frame. A semi-discrete method for (2.22)–(2.26) is concerned only with the spatial approximation of the continuum equations and begins with a discretization of the particle space. A specific finite element numerical algorithm based on this framework is presented in Section 4. We keep the description general in order to allow for alternative discrete space constructions.

Let  $d \in \{2, 3\}$  be the space dimension. The semi-discrete Lagrangian discretization is determined by two finite dimensional spaces on the initial domain  $\tilde{\Omega}$ :

- a kinematic space  $\mathcal{V} \subset [H^1(\tilde{\Omega})]^d$ , with a basis  $\{w_i\}_{i=1}^{N_{\mathcal{V}}}$ ,
- a thermodynamic space  $\mathcal{E} \subset L_2(\tilde{\Omega})$ , with a basis  $\{\phi_i\}_{i=1}^{N_{\mathcal{E}}}$ .

We discretize the position  $\{x(t)\}$  using the expansion

$$x(\tilde{x}, t) = \sum_i \mathbf{x}_i(t) w_i(\tilde{x}) = \mathbf{x}(t)^T \mathbf{w}(\tilde{x}), \quad (3.1)$$

where  $\mathbf{x}(t)$  is an unknown time-dependent vector of size  $N_{\mathcal{V}}$  and  $\mathbf{w}$  is a column vector of all the basis functions  $\{w_i\}_{i=1}^{N_{\mathcal{V}}}$ . The vector  $\mathbf{x}(t)$  represents the motion of the fluid according to

$$\Omega(t) = \{x(\tilde{x}, t) : \tilde{x} \in \tilde{\Omega}\}. \quad (3.2)$$

Note that we can define Lagrangian (moving) extensions of the kinematic and thermodynamic basis functions on  $\Omega(t)$  through the formulas  $w_i(x, t) = w_i(\tilde{x})$  and  $\phi_j(x, t) =$

$\phi_j(\tilde{x})$ , where  $x$  is the position of particle  $\tilde{x}$  at time  $t$ . Due to (2.2), these moving bases are constant along particle trajectories and therefore have zero material derivatives

$$\frac{dw_i}{dt} = 0 \quad \text{and} \quad \frac{d\phi_j}{dt} = 0. \quad (3.3)$$

The corresponding spaces will be denoted by  $\mathcal{V}(t)$  and  $\mathcal{E}(t)$  respectively.

A mild restriction on the space  $\mathcal{V}$ , expressing the fact that we can represent exactly the initial geometry, is the requirement that there is an initial coefficient vector  $\mathbf{x}(t_0)$ , such that

$$x(\tilde{x}, t_0) = \mathbf{x}(t_0)^T \mathbf{w}(\tilde{x}) = \tilde{x} \quad \forall \tilde{x} \in \tilde{\Omega}.$$

This vector provides also the initial conditions for the unknown  $\mathbf{x}(t)$ .

The discrete velocity field corresponding to the motion (3.1) is given by

$$v(\tilde{x}, t) = \sum_i \frac{d\mathbf{x}_i}{dt}(t) w_i(\tilde{x}) = \mathbf{v}(t)^T \mathbf{w}(\tilde{x}), \quad \text{i.e.} \quad \mathbf{v} = \frac{d\mathbf{x}}{dt}$$

as in (2.3). Note that we can also think of the velocity as a function on  $\Omega(t)$  with the expansion  $v(x, t) = \sum_i \frac{d\mathbf{x}_i}{dt}(t) w_i(x, t)$  using the same coordinates, but in the moving kinematic basis. We can also introduce the Jacobian of the discrete motion

$$\tilde{J}(\tilde{x}, t) = \nabla_{\tilde{x}} x = \sum_i \mathbf{x}_i(t) \nabla w_i(\tilde{x}).$$

Since both  $v$  and  $\tilde{J}$  are defined as in the continuous case (by differentiating (3.1)), we still have (2.5) as well as the GCL (2.6) on semi-discrete level.

**REMARK 1.** *Not all discretization methods preserve the GCL on semi-discrete level. For example, many schemes such as [2, 3, 17, 18] approximate the velocity divergence in the center of a zone through the time rate of change of volume*

$$\frac{1}{|\Omega(t)|} \frac{d|\Omega(t)|}{dt} = \nabla \cdot v. \quad (3.4)$$

*Though (3.4) is equivalent to (2.6) on quadrilateral meshes this is no longer the case on general 3D grids, see Section 5.1.*

Given initial density field  $\rho_0(\tilde{x}) = \rho(\tilde{x}, t_0)$ , we use the strong mass conservation principle (2.10) to define the density for all time:

$$\rho(\tilde{x}, t) = \rho_0(\tilde{x}) / |\tilde{J}(\tilde{x}, t)| \quad (3.5)$$

which as stated previously implies that the mass in every Lagrangian volume is preserved exactly.

We formulate the discrete momentum conservation equation by applying a variational formulation to the continuous equation (2.22). Using a Galerkin approach (at a given time  $t$ ) we multiply (2.22) by a moving basis test function  $w_j \in \mathcal{V}(t)$  and integrate over  $\Omega(t)$ :

$$\int_{\Omega(t)} \rho \frac{dv}{dt} \cdot w_j = \int_{\Omega(t)} (\nabla \cdot \sigma) \cdot w_j. \quad (3.6)$$

Performing integration by parts on the right hand side, we obtain

$$\int_{\Omega(t)} \rho \frac{dv}{dt} \cdot w_j = - \int_{\Omega(t)} \sigma : \nabla w_j + \int_{\partial\Omega(t)} n \cdot \sigma \cdot w_j, \quad (3.7)$$

where  $n$  is the outward pointing unit normal vector of the surface  $\partial\Omega(t)$ . Assuming the boundary integral term vanishes (which is the case e.g. for boundary conditions  $v \cdot n = 0$  and  $\sigma = -pI$ ) and expanding the velocity in the moving basis gives us

$$\sum_i \frac{d\mathbf{v}_i}{dt} \int_{\Omega(t)} \rho w_i \cdot w_j = - \int_{\Omega(t)} \sigma : \nabla w_j. \quad (3.8)$$

In other words,

$$\mathbf{M}_V \frac{d\mathbf{v}}{dt} = - \int_{\Omega(t)} \sigma : \nabla \mathbf{w}. \quad (3.9)$$

where  $\mathbf{M}_V$  is the *kinematic mass matrix* which is defined by the integral

$$\mathbf{M}_V \equiv \int_{\Omega(t)} \rho \mathbf{w} \mathbf{w}^T. \quad (3.10)$$

An important feature of our approach is that this mass matrix is independent of time due to (2.11) and (3.3):

$$\frac{d\mathbf{M}_V}{dt} = \frac{d}{dt} \int_{\Omega(t)} \rho \mathbf{w} \mathbf{w}^T = \int_{\Omega(t)} \rho \frac{d}{dt} (\mathbf{w} \mathbf{w}^T) = 0. \quad (3.11)$$

The thermodynamic discretization starts with the expansion of the internal energy in the basis  $\{\phi_j\}$ :

$$e(\tilde{x}, t) = \sum_j \mathbf{e}_j(t) \phi_j(\tilde{x}) = \mathbf{e}(t)^T \boldsymbol{\phi}(\tilde{x}),$$

where  $\mathbf{e}(t)$  is an unknown time-dependent vector of size  $N_\varepsilon$  and  $\boldsymbol{\phi}(\tilde{x})$  is a column vector of all the basis functions  $\{\phi_j\}_{j=1}^{N_\varepsilon}$ . The internal energy can also be expressed in the moving thermodynamic basis:  $e(x, t) = \sum_j \mathbf{e}_j(t) \phi_j(x, t)$ .

Consider a weak formulation of the energy conservation equation (2.24) obtained by multiplying it by  $\phi_i$  and integrating over the domain  $\Omega(t)$ :

$$\int_{\Omega(t)} \left( \rho \frac{de}{dt} \right) \phi_i = \int_{\Omega(t)} (\sigma : \nabla v) \phi_i. \quad (3.12)$$

Expressing the energy in the moving thermodynamic basis gives:

$$\sum_j \frac{d\mathbf{e}_j}{dt} \int_{\Omega(t)} \rho \phi_j \phi_i = \int_{\Omega(t)} (\sigma : \nabla v) \phi_i.$$

In other words,

$$\mathbf{M}_\varepsilon \frac{d\mathbf{e}}{dt} = \int_{\Omega(t)} (\sigma : \nabla \mathbf{v}) \boldsymbol{\phi}. \quad (3.13)$$

where  $\mathbf{M}_\mathcal{E}$  is the *thermodynamic mass matrix* which is defined by the integral

$$\mathbf{M}_\mathcal{E} \equiv \int_{\Omega(t)} \rho \phi \phi^\top. \quad (3.14)$$

Analogous to the kinematic case, we can use the fact that the thermodynamic basis functions have zero material derivatives to conclude that  $\mathbf{M}_\mathcal{E}$  is independent of time.

We now introduce an  $N_\mathcal{V} \times N_\mathcal{E}$  rectangular matrix  $\mathbf{F}$  that connects the kinematic and thermodynamic spaces:

$$\mathbf{F}_{ij} = \int_{\Omega(t)} (\sigma : \nabla w_i) \phi_j. \quad (3.15)$$

The stress tensor  $\sigma$  is defined using the equation of state and the above density and internal energy fields:

$$\sigma(x, t) = -EOS(\rho(x, t), e(x, t))I.$$

By simply changing the above evaluation, our approach can handle general stresses, including strength models and artificial viscosity terms, see Section 6.

Given these definitions, we can now summarize the general semi-discrete Lagrangian conservation laws in the following simple form:

$$\text{Momentum Conservation:} \quad \mathbf{M}_\mathcal{V} \frac{d\mathbf{v}}{dt} = -\mathbf{F} \cdot \mathbf{1}, \quad (3.16)$$

$$\text{Energy Conservation:} \quad \mathbf{M}_\mathcal{E} \frac{d\mathbf{e}}{dt} = \mathbf{F}^\top \cdot \mathbf{v}, \quad (3.17)$$

$$\text{Equation of Motion:} \quad \frac{d\mathbf{x}}{dt} = \mathbf{v}. \quad (3.18)$$

The vector  $\mathbf{1}$  above is the representation of the constant one in the thermodynamic basis  $\{\phi_i\}$  (we assume that  $1 \in \mathcal{E}$ ).

**THEOREM 3.1.** *The general semi-discrete Lagrangian method (3.16)–(3.18) has the following properties:*

- *exact geometric conservation law (2.6).*
- *exact mass conservation.*
- *exact total energy conservation.*

*This is a general result valid for any choice of the kinematic and thermodynamic spaces provided that they contain the vector field  $\tilde{\mathbf{x}}$  and the constant 1, respectively.*

*Proof.* The exact GCL and mass conservation were already discussed in the beginning of this section.

Regarding the total energy conservation, note that the formulas for the total internal and kinetic energies (2.15) and (2.16) can be expressed in the semi-discrete settings as:

$$IE(t) = \mathbf{1} \cdot \mathbf{M}_\mathcal{E} \cdot \mathbf{e}, \quad KE(t) = \frac{1}{2} \mathbf{v} \cdot \mathbf{M}_\mathcal{V} \cdot \mathbf{v}.$$

Therefore the rate of change of the total discrete energy is

$$\frac{dE}{dt} = \frac{d}{dt} \left( \frac{1}{2} \mathbf{v} \cdot \mathbf{M}_\mathcal{V} \cdot \mathbf{v} + \mathbf{1} \cdot \mathbf{M}_\mathcal{E} \cdot \mathbf{e} \right).$$



Using the fact that both the kinematic and thermodynamic mass matrices are symmetric and independent of time, as well as equations (3.16) and (3.17), we get

$$\frac{dE}{dt} = \mathbf{v} \cdot \mathbf{M}_V \cdot \frac{d\mathbf{v}}{dt} + \mathbf{1} \cdot \mathbf{M}_E \cdot \frac{d\mathbf{e}}{dt} = -\mathbf{v} \cdot \mathbf{F} \cdot \mathbf{1} + \mathbf{1} \cdot \mathbf{F}^T \cdot \mathbf{v} = 0.$$

□

REMARK 2. Let  $\mathbf{c} = \mathbf{c}^T \mathbf{w} \in \mathcal{V}$  be a vector which is constant in time and consider the change of the total momentum in the direction of  $\mathbf{c}$ . By (2.11) and (3.16), we have

$$\frac{d}{dt} \left( \mathbf{c} \cdot \int_{\Omega(t)} \rho \mathbf{v} \right) = \mathbf{c} \cdot \mathbf{M}_V \frac{d\mathbf{v}}{dt} = -\mathbf{c} \cdot \mathbf{F} \cdot \mathbf{1} = \int_{\Omega(t)} \sigma : \nabla \mathbf{c} = 0.$$

Thus, the total momentum (in any direction) is also being conserved on a semi-discrete level, provided that constant fields are representable in  $\mathcal{V}$ .

**4. Finite Element Lagrangian Discretization.** In this section we describe a finite element numerical algorithm based on the general semi-discrete Lagrangian discretization method from Section 3. The main feature of our approach is the use of high-order kinematic and thermodynamic approximation spaces defined on curvilinear meshes.

**4.1. Particle Motion and Geometry Reconstruction.** We start with some geometric considerations related to the choice of the finite element kinematic discretization space  $\mathcal{V}$  and the definition of the deformed domain  $\Omega(t)$ .

A natural way to discretize the motion of the whole medium is to describe it through the motion of only a finite number of particles. In practice, we decompose the spatial domain  $\Omega(t)$  at the initial time  $t = t_0$  into a set of non-overlapping, discrete volumes  $\{\Omega_z(t_0)\}$  called zones (or elements) and associate particles with them, see Figure 4.1. The union of these discrete zones forms the initial computational domain  $\tilde{\Omega}$  which may, in general, be an approximation of the exact initial domain.

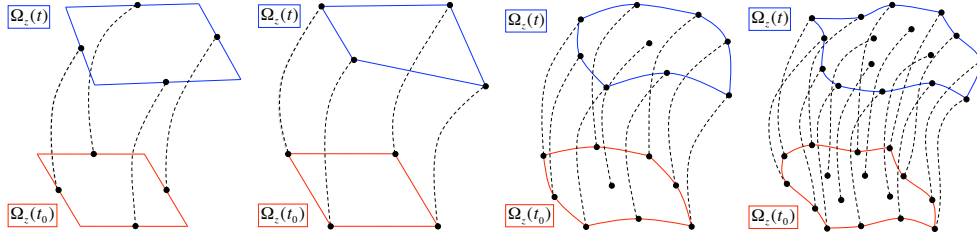


FIG. 4.1. A zone  $\Omega_z(t)$  reconstructed from the evolution of only a few of its points (particles) indicated by black circles. Shown are several different choices corresponding to (left to right) Crouzeix-Raviart,  $Q_1$ ,  $Q_2$  and  $Q_3$  finite elements. Note that the reconstruction with Crouzeix-Raviart elements is not unique and that the zone boundaries are curved in the  $Q_2$  and  $Q_3$  cases.

After evolving the particles in time, the zones  $\Omega_z(t)$  are reconstructed based on the locations of the particles associated with them (vertices, edge midpoints, etc.), thus defining the moved mesh  $\Omega(t)$ . Note that this reconstruction process introduces a *geometric error* (which should vanish under refinement), since the computational mesh will be only an approximation to the true geometry of the exact domain, even if the particle trajectories are exact.

The presence of this built-in geometric error motivates the use of high-order elements, as the  $Q_2$  and  $Q_3$  elements shown in Figure 4.1, since such elements have more degrees of freedom on the zone boundaries, allowing them to better represent smooth deformations. High-order elements are also advantageous in representing initial curvature (e.g. at boundaries and interfaces) as well as curvature naturally developing in the flow, as illustrated with the exact solutions of two classical test problems in Figure 4.2.

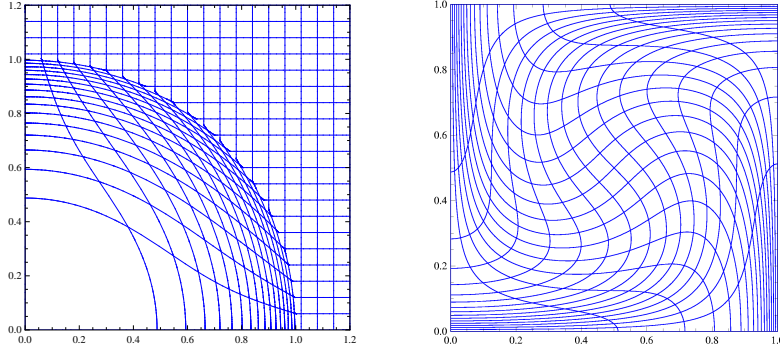


FIG. 4.2. An initial Cartesian mesh deformed according to the exact solutions of the Sedov blast wave (left) and the Taylor-Green vortex (right). See Section 8.

In Section 3 we described a general functional reconstruction approach (3.2) based on abstract particle locations represented by the expansion coefficients  $\mathbf{x}(t)$ . In the rest of this section we detail a natural way to define a local reconstruction through the finite element method (FEM). In the settings of Section 3 this amounts to defining the basis for the space  $\mathcal{V}$  by local construction on each zone.

**4.2. Curvilinear Zone Geometry.** The finite element space construction begins with definitions on the reference element  $\hat{\Omega}_z$ , e.g. the unit square in 2D or the unit cube in 3D. Throughout the remainder of this paper, all quantities which are defined with respect to the reference element coordinate system will be accented with a "hat" symbol.

We consider a basis on the reference element  $\{\hat{\eta}(\hat{x})\}_{i=1}^{N_v}$  which is nodal, i.e. there is a set of points called nodes  $\{\hat{p}_i\}_{i=1}^{N_v}$  such that  $\hat{\eta}_i(\hat{p}_j) = \delta_{ij}$  where  $\delta_{ij}$  is the Kronecker delta symbol. The points  $\{\hat{p}_i\}$  represent the fixed particle locations on  $\hat{\Omega}_z$  and  $\hat{\eta}_i$  is the (high-order) nodal basis function associated with particle  $i$  (see Figure 4.3). Given the particle locations  $\{x_{z,i}(t)\}$  for a zone  $\Omega_z(t)$ , we reconstruct the zone by defining the curvilinear zone mapping

$$\Phi_z(\hat{x}, t) = \sum_{i=1}^{N_v} x_{z,i}(t) \hat{\eta}_i(\hat{x}), \quad (4.1)$$

which is defined so that it maps the reference nodes  $\{\hat{p}_i\}$  to the particle locations of the zone (see Figure 4.1):

$$\Phi_z(\hat{p}_i, t) = x_{z,i}(t), \quad i = 1, \dots, N_v.$$

Based on this reconstruction, the volume occupied by  $\Omega_z(t)$  is image of the reference zone  $\hat{\Omega}_z$  under the map  $\Phi_z$ :

$$\Omega_z(t) = \{x = \Phi_z(\hat{x}, t) : \hat{x} \in \hat{\Omega}_z\}.$$

For the case of a traditional two-dimensional  $Q_1$  zone geometry consisting of four vertices connected by straight lines, the mapping  $\Phi_z$  is bilinear. We propose to use high-order mappings such as  $Q_2$  (biquadratic) which produce zones with curvilinear geometry as shown in Figure 4.4. In this case, the reference zone is the unit square  $\hat{\Omega}_z = [0, 1] \times [0, 1]$ , the set of nodes is

$$\begin{array}{lll} \hat{p}_1 = (0, 0) & \hat{p}_2 = (1, 0) & \hat{p}_3 = (1, 1) \\ \hat{p}_4 = (0, 1) & \hat{p}_5 = (0.5, 0) & \hat{p}_6 = (1, 0.5) \\ \hat{p}_7 = (0.5, 1) & \hat{p}_8 = (0, 0.5) & \hat{p}_9 = (0.5, 0.5), \end{array}$$

and the  $Q_2$  nodal basis is given by

$$\begin{aligned} \hat{\eta}_1(\hat{x}, \hat{y}) &= (1 - \hat{x})(1 - 2\hat{x})(1 - \hat{y})(1 - 2\hat{y}) & \hat{\eta}_2(\hat{x}, \hat{y}) &= \hat{x}(2\hat{x} - 1)(1 - \hat{y})(1 - 2\hat{y}) \\ \hat{\eta}_3(\hat{x}, \hat{y}) &= \hat{x}(2\hat{x} - 1)\hat{y}(2\hat{y} - 1) & \hat{\eta}_4(\hat{x}, \hat{y}) &= (1 - \hat{x})(1 - 2\hat{x})\hat{y}(2\hat{y} - 1) \\ \hat{\eta}_5(\hat{x}, \hat{y}) &= 4\hat{x}(1 - \hat{x})(1 - \hat{y})(1 - 2\hat{y}) & \hat{\eta}_6(\hat{x}, \hat{y}) &= \hat{x}(2\hat{x} - 1)4\hat{y}(1 - \hat{y}) \\ \hat{\eta}_7(\hat{x}, \hat{y}) &= 4\hat{x}(1 - \hat{x})\hat{y}(2\hat{y} - 1) & \hat{\eta}_8(\hat{x}, \hat{y}) &= (1 - \hat{x})(1 - 2\hat{x})4\hat{y}(1 - \hat{y}) \\ \hat{\eta}_9(\hat{x}, \hat{y}) &= 4\hat{x}(1 - \hat{x})4\hat{y}(1 - \hat{y}). \end{aligned}$$

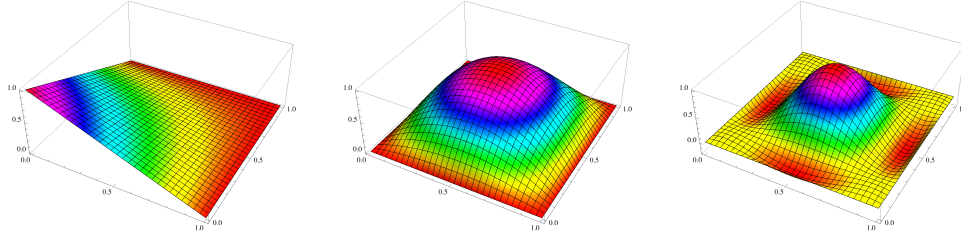


FIG. 4.3. Examples of 2D kinematic space basis functions on the reference zone: a standard  $Q_1$  bilinear function (left), a  $Q_2$  biquadratic function (center) and a  $Q_4$  biquartic function, (right).

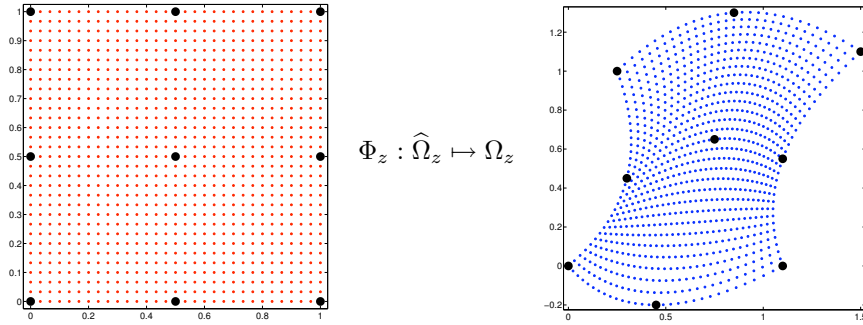


FIG. 4.4. Example of a  $Q_2$  biquadratic mapping from a reference zone (left) to a Lagrangian zone (right) defined by the locations of the 9 Lagrangian particles (black dots).

The global FEM space  $\mathcal{V}(t)$  (see Section 3) is defined by identifying the particles that share the same physical location, i.e. particles at common zone boundaries. With any global particle  $p$  we associate  $d$  vector basis functions  $w_i$  of the form

$$(\eta_p, 0, 0) \quad (0, \eta_p, 0) \quad (0, 0, \eta_p) \quad \text{in 3D}.$$

The scalar function  $\eta_p$  is non-zero only in zones  $\Omega_z$  that contain the particle  $p$ . Restricted to  $\Omega_z$  it is defined as

$$\eta_p(x, t)|_{\Omega_z} = \hat{\eta}_j(\hat{x}), \quad \text{with } x = \Phi_z(\hat{x}, t), \quad (4.2)$$

where  $j$  is the local particle index for  $p$  in the zone  $\Omega_z$ . In this (nodal) FEM setting, the global unknown vector  $\mathbf{x}(t)$  consists of all components of all particles. Here, we defined  $\mathcal{V}(t)$  directly using the particle trajectories whereas in Section 3 we defined it through  $\mathcal{V} = \mathcal{V}(t_0)$ . Both approaches are identical. Indeed, the bases agree at  $t = t_0$  (by definition) and (4.2) implies that the material derivatives of  $w_i$  are zero which coincides with the definition used in Section 3. In particular,

$$\Phi_z(\hat{x}, t) = \tilde{\Phi}(\Phi_z(\hat{x}, t_0), t). \quad (4.3)$$

**4.3. Strong Mass Conservation.** The element Jacobian matrix is defined as

$$\mathbf{J}_z = \nabla_{\hat{x}} \Phi_z, \quad (4.4)$$

and generally varies in the zone. The determinant of the Jacobian,  $|\mathbf{J}_z| \equiv \det \mathbf{J}_z$ , gives a measure of volume at a specific point, since the total volume of a Lagrangian zone can be computed as

$$|\Omega_z(t)| = \int_{\hat{\Omega}_z} \det \mathbf{J}_z(t). \quad (4.5)$$

By differentiating (4.3), we get the following relation between the element Jacobian and the Jacobian of the Lagrangian transformation from Section 3:

$$\mathbf{J}_z(t) = \mathbf{J}_z(t_0) \tilde{\mathcal{J}}(t). \quad (4.6)$$

A fundamental postulate of the Lagrangian description of hydrodynamics is the fact that the total mass contained within a discrete volume element  $\Omega_z$  does not change in time. In other words, if we introduce the “zonal mass”

$$\mathbf{m}_z \equiv \int_{\Omega_z(t)} \rho \quad \text{then} \quad \frac{d\mathbf{m}_z}{dt} = 0.$$

In both SGH and CCH Lagrangian formulations, the zonal mass is a fundamental quantity and is used to define the evolution of the density as the ratio of the zonal mass to the current volume of the zone. In practice, this is known as “mass conservation by fiat” and it means that the point wise form of the mass conservation equation in (2.23) is not explicitly discretized.

In contrast, we use our general framework to eliminate the density through the *strong mass conservation principle* (3.5), which in this case takes the form

$$\rho(t) |\det \mathbf{J}_z(t)| = \rho(t_0) |\det \mathbf{J}_z(t_0)|. \quad (4.7)$$

Note that the density defined by this equation is not a finite element (or polynomial) function.

The principle of strong mass conservation can be viewed as a generalization of zonal mass conservation as well as the “sub-zonal mass” concept introduced in [17]. It allows us to define density at any point in time and space as a *function* which is a critical component of our approach. An alternative approach is to define high-order mass moments, e.g. by projecting the above density in a discontinuous finite element space as in [36].

**4.4. Finite Element Kinematics.** The momentum conservation equation is discretized following the general framework of Section 3 based on the finite element kinematic space from Section 4.2.

The locality of the finite element basis implies that the global kinematic mass matrix is sparse and can be computed through standard finite element assembly procedure from zonal mass matrices:

$$\mathbf{M}_V = \text{Assemble}(\mathbf{M}_{V,z}).$$

The process of global assembly is analogous to the concept of “nodal accumulation” that is used in a traditional SGH method where a quantity at a node is defined to be the sum of contributions from all of the zones which share this node.

Note that  $\mathbf{M}_V$  is symmetric positive definite and block-diagonal (with identical blocks). It is also well-conditioned, which implies that simple conjugate gradient iteration can be used to solve the momentum equation iteratively with optimal efficiency.

Since the kinematic mass matrix is independent of time, see (3.11), we compute and store  $\mathbf{M}_V$  only in the beginning of the simulation. In practice, the local mass matrices  $\mathbf{M}_{V,z}$  are computed by transforming the integrals to the reference element and applying a quadrature rule.

**4.5. Finite Element Thermodynamics.** Since the kinematic degrees of freedom overlap between the zones, it is natural to understand the momentum conservation equation in a global (continuous) sense. In contrast, the equation of state is local, underlining the local character of the density, pressure and internal energy. Therefore, we argue that the thermodynamic space  $\mathcal{E}$  should be discontinuous to allow for restriction of the internal energy conservation equation to the computational zones.

Specifically, to define  $\mathcal{E}(t)$  we introduce a thermodynamic basis  $\{\hat{\phi}_i\}$  on the reference element and define the global moving basis  $\{\phi_j\}$  through the mapping  $\Phi_z$ . This is done zone-by-zone keeping the zonal degrees of freedom independent, which produces a basis that is discontinuous across zone boundaries. For example, if  $j$  is a global degree of freedom corresponding to a local index  $i$  in a zone  $\Omega_z$ , then  $\phi_j$  is zero outside of  $\Omega_z$  and

$$\phi_j(x, t)|_{\Omega_z} = \hat{\phi}_i(\hat{x}), \quad \text{with } x = \Phi_z(\hat{x}, t). \quad (4.8)$$

Following the general framework of Section 3 we use  $\mathcal{E}(t)$  to discretize the energy conservation equation, locally on each zone. As with the kinematic mass matrix, we can consider the thermodynamic mass matrix as being assembled from the local mass matrices on each individual zone

$$\mathbf{M}_E = \text{Assemble}(\mathbf{M}_{E,z}).$$

However, due to the discontinuous nature of the thermodynamic basis, there is no sharing of degrees of freedom across zone boundaries and so the “assembled” thermodynamic mass matrix is *block diagonal* with each block being purely local matrix on each zone. Since these matrices are independent of time, we compute and store the inverses  $\mathbf{M}_{E,z}^{-1}$  at the beginning of the simulation. In practice, the local mass matrices  $\mathbf{M}_{E,z}$  are computed by transforming the integrals to the reference element and applying a quadrature rule.

Note that continuous finite element thermodynamic spaces can also be handled in our framework, though this will introduce interaction between the energies in different zones, and lead to a global matrix  $\mathbf{M}_E$ .

**4.6. The Generalized Force Matrix.** As with the previously defined mass matrices, the matrix  $\mathbf{F}$  from (3.15), which we call the *generalized force matrix* can be assembled from zonal contributions:

$$\mathbf{F} = \text{Assemble}(\mathbf{F}_z)$$

where

$$(\mathbf{F}_z)_{ij} \equiv \int_{\Omega_z(t)} (\sigma : \nabla w_i) \phi_j.$$

This local rectangular matrix is the high-order generalization of the "corner force" concept described in [17]. It represents the hydrodynamic force contributions from a given zone to a given shared kinematic degree of freedom as well as the work done by the velocity gradient in the energy equation.

Evaluating  $\mathbf{F}_z$  is a locally FLOP-intensive calculation that forms the computational kernel of our finite element discretization method. Specifically, we transform each zone back to the reference element where we apply a quadrature rule with points  $\{\hat{q}_k\}$  and weights  $\{\alpha_k\}$ :

$$(\mathbf{F}_z)_{ij} \approx \sum_k \alpha_k \hat{\sigma}(\hat{q}_k) : \mathbf{J}_z^{-1}(\hat{q}_k) \hat{\nabla} \hat{w}_i(\hat{q}_k) \hat{\phi}_j(\hat{q}_k) |\det \mathbf{J}_z(\hat{q}_k)|. \quad (4.9)$$

Note that in general, the total stress  $\sigma$  is *evaluated at each quadrature point*. In the absence of shear and artificial stresses (see Section 6), the total stress is given by  $\sigma = -pI$  and the pressure is therefore evaluated at each quadrature point through the equation of state in the evaluation of (4.9). Furthermore, the density (in an EOS call for example) is *evaluated at each quadrature point* using the strong mass conservation principle of (4.7). The notion of sampling the density and pressure as functions evaluated at zone quadrature points is a key component of our high-order discretization approach and is essential for robust behavior.

**REMARK 3.** *The use of quadrature rules to approximate the integrals in the evaluation of the zonal mass and corner force matrices is not always exact (depending on the functional form of the integrand and the order of the quadrature rule). This step therefore introduces an additional approximation to the solution of the continuum equations. In practice, we use tensor product Gauss-Legendre quadrature on quadrilateral and hexahedral meshes.*

**5. Relation to Classical Discretization Schemes.** In this section we derive some classical discretization schemes from our general framework under additional discretization assumptions.

**5.1. The Staggered Grid Method of Wilkins.** In this section we show that using a piecewise bilinear kinematic approximation and a single point quadrature rule with mass lumping, we can exactly recover the traditional staggered-grid method of Wilkins [2] as well as a variant of the method described in [18] on general quadrilateral grids.

The reference zone  $\hat{\Omega}_z$  is the unit square with vertices

$$\hat{X}_1 = (0, 0), \quad \hat{X}_2 = (1, 0), \quad \hat{X}_3 = (1, 1), \quad \hat{X}_4 = (0, 1),$$

and corresponding basis functions

$$\hat{\eta}_1(\hat{x}, \hat{y}) = (1 - \hat{x})(1 - \hat{y}), \quad \hat{\eta}_2(\hat{x}, \hat{y}) = (1 - \hat{x})\hat{y}, \quad \hat{\eta}_3(\hat{x}, \hat{y}) = \hat{x}\hat{y}, \quad \hat{\eta}_4(\hat{x}, \hat{y}) = \hat{x}(1 - \hat{y}).$$

The Jacobian matrix for a bilinear mapping to a fixed zone  $\Omega_z$  with vertices  $\{X_i = (x_i, y_i)\}_{i=1}^4$  has the form

$$\mathbf{J}_z(\hat{x}, \hat{y}) = \begin{pmatrix} J_{1,1} & J_{1,2} \\ J_{2,1} & J_{2,2} \end{pmatrix} = \begin{pmatrix} X_2 - X_1 + (X_3 - X_2 - X_4 + X_1)\hat{y} \\ X_4 - X_1 + (X_3 - X_2 - X_4 + X_1)\hat{x} \end{pmatrix}, \quad (5.1)$$

and its inverse can be expressed in terms of its adjugate:

$$\mathbf{J}_z^{-1} = \frac{1}{\det \mathbf{J}_z} \mathbf{J}_z^\perp \quad \text{where} \quad \mathbf{J}_z^\perp = \begin{pmatrix} J_{2,2} & -J_{1,2} \\ -J_{2,1} & J_{1,1} \end{pmatrix}.$$

The zonal kinematic mass matrix is

$$\mathbf{M}_{V,z} = \begin{pmatrix} \mathbf{M}_{V,z}^{xx} & \mathbf{0} \\ \mathbf{0} & \mathbf{M}_{V,z}^{yy} \end{pmatrix}, \quad \text{where} \quad (\mathbf{M}_{V,z}^{xx})_{ij} = (\mathbf{M}_{V,z}^{yy})_{ij} = \int_{\hat{\Omega}_z} \rho \hat{\eta}_i \hat{\eta}_j |\det \mathbf{J}_z|.$$

Note that the determinant of the Jacobian matrix (5.1) is a *linear* function on the reference element. Therefore (4.5) implies that the application of a simple one point quadrature rule to the mass matrix integral results in

$$\mathbf{M}_{V,z}^{xx} \approx \frac{\rho_z}{16} |\Omega_z| \begin{pmatrix} 1 & 1 & 1 & 1 \\ 1 & 1 & 1 & 1 \\ 1 & 1 & 1 & 1 \\ 1 & 1 & 1 & 1 \end{pmatrix},$$

where  $\rho_z$  denotes the value of the density at the zone center.

If we now apply “mass lumping” to  $\mathbf{M}_{V,z}^{xx}$ , the global kinematic mass matrix  $\mathbf{M}_V$  will be diagonal with entries corresponding to the so-called “nodal masses”

$$m_n = \sum_{\Omega_z \ni n} \frac{1}{4} \rho_z |\Omega_z|.$$

In other words, we can approximate the mass associated with node  $n$  by simply adding a quarter of the zone averaged mass of each zone which shares the node. This is precisely the definition of the nodal mass that is used in the method of [2].

To compute the right hand side of (3.9), we assume  $\sigma = -pI$ , and define the *corner force* vector  $\mathbf{f}_z$  at a vertex  $j$  (a rearrangement of our  $8 \times 1$  matrix  $\mathbf{F}_z$ )

$$(\mathbf{f}_z)_j = (\mathbf{f}_z^x, \mathbf{f}_z^y)_j^T = \int_{\hat{\Omega}_z} p \nabla \eta_j = \int_{\hat{\Omega}_z} p (\mathbf{J}_z^{-1} \nabla \hat{\eta}_j) |\det \mathbf{J}_z|. \quad (5.2)$$

Applying the same one point quadrature rule to the above integral and inserting the gradients of the bilinear basis functions

$$\nabla \hat{\eta}_1 = (\hat{y} - 1, \hat{x} - 1) \quad \nabla \hat{\eta}_2 = (\hat{y} - 1, -\hat{x}) \quad \nabla \hat{\eta}_3 = (\hat{y}, \hat{x}) \quad \nabla \hat{\eta}_4 = (-\hat{y}, 1 - \hat{x}),$$

as well as the expressions for the term  $\mathbf{J}_z^\perp$ , we arrive at the values

$$\mathbf{f}_z^x = \frac{p_z}{2} (y_2 - y_4, y_3 - y_1, y_4 - y_2, y_1 - y_3), \quad \mathbf{f}_z^y = \frac{p_z}{2} (x_4 - x_2, x_1 - x_3, x_2 - x_4, x_3 - x_1).$$

Here  $p_z$  denotes the value of the pressure field  $p$  evaluated at the center of the zone. These “corner forces” contribute to the total pressure gradient force acting on node  $n$  by

$$f_{x,n} = \sum_{\Omega_z \ni n} \mathbf{f}_z^x, \quad f_{y,n} = \sum_{\Omega_z \ni n} \mathbf{f}_z^y,$$

which is precisely the formula for the so called “HEMP” pressure gradient operator of [2]. We point out that this is also algebraically identical to the compatible hydro method for calculating the pressure gradient as shown in [17] (see Figure 5.1). Indeed, in the notation of Figure 5.1, we have

$$(\vec{n}_1 - \vec{n}_2)p_1 + (\vec{n}_2 - \vec{n}_3)p_2 + (\vec{n}_3 - \vec{n}_4)p_3 + (\vec{n}_4 - \vec{n}_1)p_4 = (p_1 - p_4)\vec{n}_1 + (p_2 - p_1)\vec{n}_2 + (p_3 - p_2)\vec{n}_3 + (p_4 - p_3)\vec{n}_4.$$

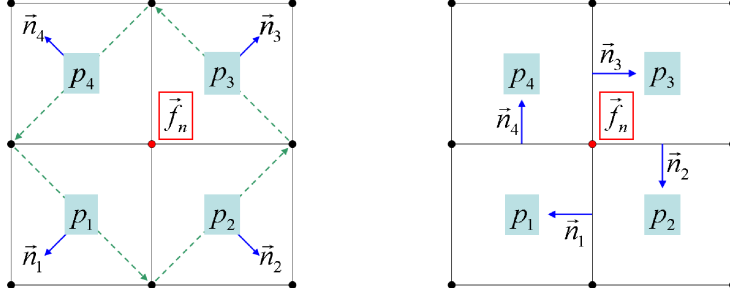


FIG. 5.1. Schematic depiction of control volume differencing schemes used for computing the node centered gradient of a cell centered pressure. On the left is the so called HEMP approach of Wilkins, on the right is the compatible finite difference approach of Caramana et. al. Both approaches are algebraically identical for an arbitrary quadrilateral grid and can be derived from a general FEM approach.

We remark that for constant pressure, the integrand of (5.2) is a bilinear function and therefore a simple one point quadrature is enough for the *exact* computation of the corner forces. This is not the case in 3D, where the integrand is a triquadratic function that requires an 8-point Gaussian rule for exact integration.

**5.2. The Compatible Hydro Method of Caramana et. al.** In [16, 17, 18], the authors introduce the notion of sub-zonal Lagrangian “corner masses” and corresponding “corner forces” which serve two purposes: they are used to compute work terms for updating the internal energy in a manner which conserves total energy algebraically and the corner masses are used to infer sub-zonal pressure changes which are then used to compute internal zone forces designed to resist hourglass mode deformations and Lagrangian mesh instabilities.

Consider the specific approximation choices used in Section 5.1 along with the additional choice of a piecewise constant internal energy basis (i.e. a single thermodynamic degree of freedom per zone). For each zone, our general high-order semi-discrete energy conservation law reduces to the form

$$\mathbf{M}_\varepsilon \frac{de}{dt} = \int_{\Omega_z(t)} (\sigma : \nabla v) \phi \quad \mapsto \quad m_z \frac{de_z}{dt} = \int_{\Omega_z(t)} p \nabla \cdot v$$

where  $m_z$  is the zonal mass and  $e_z$  is the zone averaged value of the internal energy. Our method can be viewed as a high-order generalization of the energy conserving compatible formulation of [17] by noting that

$$\mathbf{f}_z = \int_{\Omega_z(t)} p \nabla \cdot \mathbf{w},$$



which is a collection of corner forces, c.f Section 5.1. The total change in energy is therefore given by the inner product

$$\mathbf{f}_z \cdot \mathbf{v}_z = \sum_{j=1}^4 f_j \cdot v_j$$

For the specific approximation choices of Section 5.1,  $\mathbf{f}_z$  are the corner forces for each vertex of the zone.

In our evaluation of the generalized force matrix at each quadrature point in (4.9), we are treating the density and pressure (via the EOS) as functions that vary within the zone which can be viewed as a high order generalization of the "corner mass" and sub-zonal pressure concepts. Note that in [18] the corner masses are defined in terms of four Lagrangian sub-volumes associated with the four vertices of a quadrilateral zone and that the sub-zonal pressures are inferred by extrapolation of the cell averaged pressure using the changes in these sub-volumes. In contrast, our approach evaluates the pressure directly via the EOS at each quadrature point using the density from strong mass conservation via (4.7).

**6. Artificial Viscosity.** To facilitate the case of shock wave propagation, we now introduce a general tensor artificial viscosity to our semi-discrete equations. The method of artificial viscosity, as originally introduced by Von Neumann and Richtmyer [5], augments the discrete Euler equations with a diffusion term which is scaled by a special mesh dependent, non-linear coefficient. Improvements to this basic technique include the use of a Van Leer type "monotonic limiter" [37] and an additional linear term due to Landshoff [38] which act to keep the artificial diffusion length of the shock front to a minimum while preventing spurious Gibbs like oscillations in the vicinity of the shock. We introduce a tensor artificial viscosity (c.f. [22]) by adding an artificial stress tensor  $\sigma_a$  to the total stress tensor  $\sigma$ :

$$\sigma(x) = -p(x)I + \sigma_a(x).$$

We emphasize at this point that the artificial stress (as well as the total stress) is in general a *function* of the spatial coordinates and therefore varies inside a zone.

We denote the symmetrized velocity gradient as

$$\varepsilon(v) \equiv \frac{1}{2}(\nabla v + v \nabla) \quad (6.1)$$

which can be spectrally decomposed as

$$\varepsilon(v) = \sum_k \lambda_k s_k \otimes s_k, \quad s_i \cdot s_j = \delta_{ij}, \quad \lambda_1 \leq \dots \leq \lambda_d \quad (6.2)$$

where  $\lambda_k$  and  $s_k$  are the eigenvalues and eigenvectors respectively, sorted from smallest to largest eigenvalue. Note that according to the definition of directional measure of compression (6.4),  $s_1$  is the direction of "maximal compression" (see (6.5)).

We consider a set of artificial viscosity types as summarized in Table 6.1. In general, the artificial stress tensor is defined in terms of a directional viscosity coefficient  $\mu_s$  (see Section 6.1) and a velocity gradient tensor. For Type 1 and Type 2 from Table 6.1, the directional vector  $s$  is defined to be  $s_1$ . Each form of the artificial stress satisfies the inequality

$$\sigma_a(x) : \nabla v(x) \geq 0, \quad \forall x,$$

which is an essential property for ensuring a strictly dissipative artificial viscosity, ensuring positive entropy production. Note that all  $\sigma_a$  from Table 6.1 are symmetric except Type 1,  $\mu_s \nabla v$ , for the case of  $\nabla \times v \neq 0$ .

Artificial Stress Type	Definition	Symmetric
Type 1	$\sigma_a = \mu_{s_1} \nabla v$	No
Type 2	$\sigma_a = \mu_{s_1} \varepsilon(v)$	Yes
Type 3	$\sigma_a = \mu_{s_k} \lambda_k s_k \otimes s_k$	Yes
Type 4	$\sigma_a = \sum_k \mu_{s_k} \lambda_k s_k \otimes s_k$	Yes

TABLE 6.1

Summary of artificial stress types.

**6.1. Directional Viscosity Coefficient.** Following [22], we consider a general viscosity coefficient of the form

$$\mu_s(x) \equiv \rho \{q_2 \ell_s^2 |\Delta_s v| + q_1 \psi_0 \psi_1 \ell_s c_s\} \quad (6.3)$$

where  $q_1$  and  $q_2$  are linear and quadratic scaling coefficients respectively,  $c_s$  is the speed of sound evaluated at point  $x$ , and  $\ell_s = \ell_s(x)$  is a "directional length scale" defined in the direction of the vector  $s$  (see Section 6.2) evaluated at point  $x$ .

The directional measure of compression (or velocity jump term)  $\Delta_s v$  is defined as

$$\Delta_s v = \frac{s \cdot \nabla v \cdot s}{s \cdot s} = \frac{s \cdot \varepsilon(v) \cdot s}{s \cdot s} = \frac{d(v \cdot s)}{ds}. \quad (6.4)$$

In other words, the measure of compression is defined as a directional derivative of the velocity in the direction given by the vector  $s$ . The following identity holds:

$$\min_{|s|=1} \frac{s \cdot \varepsilon(v) \cdot s}{s \cdot s} = \frac{s_1 \cdot \varepsilon(v) \cdot s_1}{s_1 \cdot s_1} = \lambda_1 \quad (6.5)$$

which means that the direction  $s_1$  minimizes  $\Delta_s v$  over all unit directions  $s$  and the measure of compression in direction  $s_1$  is given by  $\lambda_1$ .

Finally, we define a "compression switch" which causes the artificial viscosity to vanish at points in expansion

$$\psi_1 = \begin{cases} 1, & \Delta_s v < 0 \\ 0, & \Delta_s v \geq 0 \end{cases}$$

as well as a "vorticity measure" which causes the artificial to vanish for purely vortical flows

$$\psi_0 = \frac{|\nabla \cdot v|}{\|\nabla v\|}.$$

**6.2. Directional Length Scale.** Artificial viscosities require the definition of a grid (mesh) dependent length scale. In many SGH formulations, this length scale is a simple piecewise constant quantity which is computed as the square (cube) root of the zone area (volume). More sophisticated treatments incorporate knowledge of the shock velocity to determine the length scale or define the length scale as more than

just a single constant value in the zone (e.g. [20]). Choices made in defining this scale can have serious consequences with regard to the "mesh imprinting" phenomenon that is the bane of many Lagrangian methods.

We define the length scale as a function (i.e. a length scale field) defined at a spatial coordinate  $x$  in terms of a direction vector  $s$ , relative to an initial length scale field  $\ell_0(\tilde{x})$  defined on the initial domain  $\tilde{\Omega}$ . Functionally this can be written through the Jacobian  $\tilde{J}$  of the Lagrangian transformation  $\tilde{\Phi} : \tilde{\Omega} \rightarrow \Omega(t)$  as either

$$\ell_s(x) = \ell_0 \frac{|s|}{|\tilde{J}^{-1}s|}, \quad (6.6)$$

or

$$\ell_s(x) = \ell_0 \frac{|\tilde{J}^T s|}{|s|}. \quad (6.7)$$

The differences between the definitions of (6.6) and (6.7) are illustrated in Figure 6.1. Our default choice is to use first definition (6.6). In practice, the Jacobian matrix  $\tilde{J}$  is computed zone-by-zone via the zone Jacobians  $\mathbf{J}_z$  using (4.6):

$$\tilde{J}(t) = [\mathbf{J}_z(t_0)]^{-1} \mathbf{J}_z(t).$$

Note that the use of the Jacobian of the mapping from the *initial* element in (6.6) and (6.7) is essential. If, for example, we used the mapping from the reference element, or in other words if we used  $\mathbf{J}_z$  instead of  $\tilde{J}$ , the symmetry preservation properties of the solution degrade on general grids as illustrated in Figure 6.2.

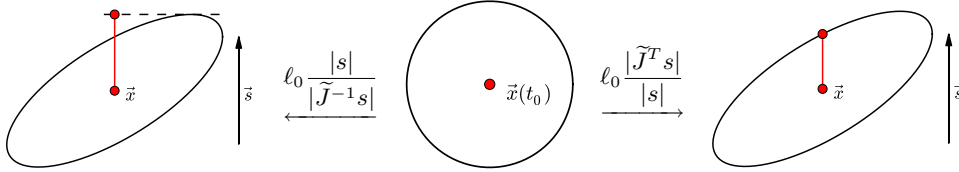


FIG. 6.1. Examples of the initial length scale field transformation from an initial zone (center) to a Lagrangian zone via (6.6) (left) and (6.7) (right).

The initial length scale field  $\ell_0(\tilde{x})$  can be defined on the initial mesh in different ways such as

- A global constant, e.g. in 2D  $\ell_0 = (\text{tot. area}/\text{num. of zones})^{1/2}$  (for initial meshes which are close to uniform).
- A smoothed version of a local mesh size function (for initial meshes with local refinement).
- A smoothed or constant function based on a given mesh direction size (for 1D problems).

For high-order methods, we divide the length scale field  $\ell_0$  by the polynomial degree of the kinematics space.

**6.3. Non-scalar tensor viscosity coefficient.** In this section we consider in detail some properties of the different types of artificial stresses we defined.

Let  $\mathbf{s}$  be a unit column vector. Then the action of the rank-1 matrix  $\mathbf{ss}^T$  is simply the projection onto the direction specified by  $\mathbf{s}$ , since  $(\mathbf{ss}^T)\mathbf{v} = (\mathbf{v} \cdot \mathbf{s})\mathbf{s}$ .

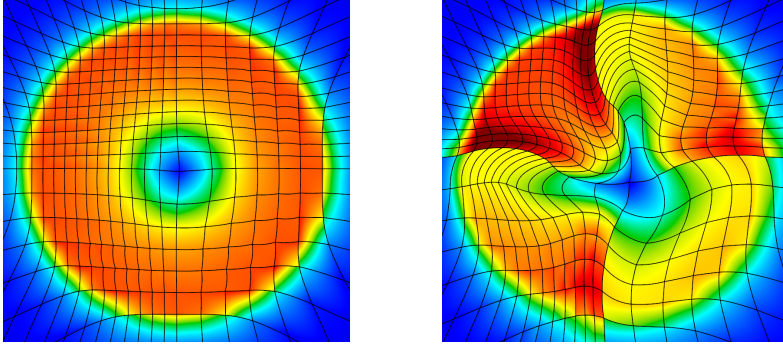


FIG. 6.2. Numerical results for the Noh implosion problem on a  $24 \times 24$  distorted grid, cf. Section 8.4, using a directional length scale defined through a mapping to initial element  $\Omega_z(t_0) \leftarrow \Omega_z(t)$  (left), versus a mapping to the reference element  $\hat{\Omega} \leftarrow \Omega_z(t)$  (right).

Now, let  $\{\mathbf{s}_k\}$  be an orthonormal basis, i.e.  $\mathbf{s}_i^T \mathbf{s}_j = \delta_{ij}$ , and consider the matrix

$$\mathbf{A} = \sum_k \lambda_k \mathbf{s}_k \mathbf{s}_k^T.$$

It is straightforward to check that  $\mathbf{A}$  is symmetric, and has eigenvalues  $\lambda_k$  with corresponding eigenvectors  $\mathbf{s}_k$ . In other words,  $\mathbf{A} = \text{diag}(\lambda)$  in the coordinate system given by  $\{\mathbf{s}_k\}$ .

Note that  $\mathbf{I} = \sum_k \mathbf{s}_k \mathbf{s}_k^T$ , and if  $\mathbf{B} = \sum_k \mu_k \mathbf{s}_k \mathbf{s}_k^T$  then

$$\mathbf{A}\mathbf{B} = \sum_k \lambda_k \mu_k \mathbf{s}_k \mathbf{s}_k^T \quad \text{and} \quad \mathbf{A} : \mathbf{B} = \text{tr}(\mathbf{A}^T \mathbf{B}) = \sum_k \lambda_k \mu_k.$$

Let us denote by  $\sigma_k$  the artificial stress of type  $k$ . Identifying the eigenvectors  $\mathbf{s}_k$  of  $\varepsilon(v)$  with the column vectors  $\mathbf{s}_k$ , we have

$$\sigma_2 = \mu \sum_k \lambda_k \mathbf{s}_k \mathbf{s}_k^T.$$

Thus, it is natural to introduce the directionally split tensor artificial viscosity stresses

$$\sigma_3 = \mu_k \lambda_k \mathbf{s}_k \mathbf{s}_k^T \quad \text{and} \quad \sigma_4 = \sum_k \mu_k \lambda_k \mathbf{s}_k \mathbf{s}_k^T.$$

The index  $k$  in  $\sigma_3$  is typically chosen to correspond to maximal compression (smallest negative eigenvalue) or to the spectral radius (eigenvalue with maximal modulus). Note that the shock entropy term is non-negative in all cases:  $\sigma_1 : \nabla \vec{v} = \mu \nabla \vec{v} : \nabla \vec{v}$ , while by symmetry

$$\sigma_2 : \nabla \vec{v} = \mu \varepsilon(\vec{v}) : \varepsilon(\vec{v}), \quad \sigma_3 : \nabla \vec{v} = \sigma_3 : \varepsilon(\vec{v}) = \mu_k \lambda_k^2, \quad \sigma_4 : \nabla \vec{v} = \sigma_4 : \varepsilon(\vec{v}) = \sum_k \mu_k \lambda_k^2.$$

Note also that unlike  $\sigma_1$ , the symmetric stresses  $\sigma_2$ ,  $\sigma_3$  and  $\sigma_4$  do not result in a block-diagonal stiffness matrix, since  $\nabla(\phi; 0) : \nabla(0; \psi) \neq 0$ , but  $\varepsilon(\phi; 0) : \varepsilon(0; \psi) \neq 0$ .

More generally, we can use arbitrary set of given orthonormal directions  $\{\mathbf{s}_k\}$ , not necessarily related to  $\varepsilon(\vec{v})$ , and define

$$\sigma_3 = \mu_k (\mathbf{s}_k^T \varepsilon(\vec{v}) \mathbf{s}_k) \mathbf{s}_k \mathbf{s}_k^T \quad \text{and} \quad \sigma_4 = \sum_k \mu_k (\mathbf{s}_k^T \varepsilon(\vec{v}) \mathbf{s}_k) \mathbf{s}_k \mathbf{s}_k^T.$$

Since  $\mathbf{s}_k^T \varepsilon(\vec{v}) \mathbf{s}_k = \sum_{i,j} (\mathbf{s}_k)_i \varepsilon(\vec{v})_{ij} (\mathbf{s}_k)_j = \mathbf{s}_k \mathbf{s}_k^T : \varepsilon(\vec{v})$ , we still have

$$\sigma_3 : \nabla \vec{v} = \mu_k (\mathbf{s}_k^T \varepsilon(\vec{v}) \mathbf{s}_k)^2 \geq 0, \quad \sigma_4 : \nabla \vec{v} = \sum_k \mu_k (\mathbf{s}_k^T \varepsilon(\vec{v}) \mathbf{s}_k)^2 \geq 0.$$

Set

$$\mathbf{M}_2 = \mu \mathbf{I} = \mu \sum_k \mathbf{s}_k \mathbf{s}_k^T, \quad \mathbf{M}_3 = \mu_k \mathbf{s}_k \mathbf{s}_k^T, \quad \mathbf{M}_4 = \sum_k \mu_k \mathbf{s}_k \mathbf{s}_k^T,$$

Then it is straightforward to check that

$$\sigma_2 = \mathbf{M}_2 \varepsilon(\vec{v}), \quad \sigma_3 = \mathbf{M}_3 \varepsilon(\vec{v}), \quad \sigma_4 = \mathbf{M}_4 \varepsilon(\vec{v}).$$

Note that the non-scalar options  $\sigma_3$  and  $\sigma_4$  require the use of the symmetrized velocity gradient in the tensor viscosity stress.

**7. Time Integration and the Fully-Discrete Approximation.** So far we have focused exclusively on the spatial discretization, but in practice one needs to also discretize the time derivatives in the nonlinear system of ODEs (3.16)–(3.18) obtained after the spatial discretization of the Euler equations. In this section we consider a general high-order temporal discretization method, and demonstrate its impact on the semi-discrete conservation laws. Specifically, let  $t \in \{t_n\}_{n=0}^{N_t}$ , and associate with each moment in time,  $t_n$ , the computational domain  $\Omega^n \equiv \Omega(t_n)$ . We identify the quantities of interest defined on  $\Omega^n$  with a superscript  $n$ .

Let  $Y = (\mathbf{v}; \mathbf{e}; \mathbf{x})$  be the hydrodynamic state vector. Then the semi-discrete conservation equations of (3.16)–(3.18) can be written in the form:

$$\frac{dY}{dt} = \mathcal{F}(Y, t),$$

where

$$\mathcal{F}(Y, t) = \begin{pmatrix} \mathcal{F}_v(\mathbf{v}, \mathbf{e}, \mathbf{x}) \\ \mathcal{F}_e(\mathbf{v}, \mathbf{e}, \mathbf{x}) \\ \mathcal{F}_x(\mathbf{v}, \mathbf{e}, \mathbf{x}) \end{pmatrix} = \begin{pmatrix} -\mathbf{M}_v^{-1} \mathbf{F} \cdot \mathbf{1} \\ \mathbf{M}_e^{-1} \mathbf{F}^T \cdot \mathbf{v} \\ \mathbf{v} \end{pmatrix}$$

Standard high-order time integration techniques (e.g. explicit Runge-Kutta methods) can be applied to this system of nonlinear ODEs. However, these standard methods may need modifications to ensure numerical stability of the scheme and to ensure exact energy conservation. An example of this is given in the next section. Note that in general, a time integration method of order  $N$  will require  $N$  evaluations of the function  $\mathcal{F}(Y, t)$ .

**7.1. The RK2-Average Scheme.** The midpoint Runge-Kutta second order scheme reads

$$Y^{n+\frac{1}{2}} = Y^n + \frac{\Delta t}{2} \mathcal{F}(Y^n, t^n)$$

$$Y^{n+1} = Y^n + \Delta t \mathcal{F}(Y^{n+\frac{1}{2}}, t^{n+\frac{1}{2}}).$$

In practice, we have observed that the above scheme may be unstable even for simple test problems. Therefore, we developed a modification of the scheme to improve its stability and to ensure total energy conservation. First, for the half time step values we compute

$$\begin{aligned}\mathbf{v}^{n+\frac{1}{2}} &= \mathbf{v}^n - (\Delta t/2) \mathbf{M}_V^{-1} \mathbf{F}^n \cdot \mathbf{1} \\ \mathbf{e}^{n+\frac{1}{2}} &= \mathbf{e}^n + (\Delta t/2) \mathbf{M}_E^{-1} (\mathbf{F}^n)^T \cdot \mathbf{v}^{n+\frac{1}{2}} \\ \mathbf{x}^{n+\frac{1}{2}} &= \mathbf{x}^n + (\Delta t/2) \mathbf{v}^{n+\frac{1}{2}}.\end{aligned}$$

Then, for the full time step values we compute

$$\begin{aligned}\mathbf{v}^{n+1} &= \mathbf{v}^n - \Delta t \mathbf{M}_V^{-1} \mathbf{F}^{n+\frac{1}{2}} \cdot \mathbf{1} \\ \mathbf{e}^{n+1} &= \mathbf{e}^n + \Delta t \mathbf{M}_E^{-1} (\mathbf{F}^{n+\frac{1}{2}})^T \cdot \bar{\mathbf{v}}^{n+\frac{1}{2}} \\ \mathbf{x}^{n+1} &= \mathbf{x}^n + \Delta t \bar{\mathbf{v}}^{n+\frac{1}{2}}.\end{aligned}$$

Here  $\mathbf{F}^n = \mathbf{F}(Y^n)$  and  $\bar{\mathbf{v}}^{n+\frac{1}{2}} = (\mathbf{v}^n + \mathbf{v}^{n+1})/2$ .

**PROPOSITION 7.1.** *The RK2-Average scheme described above conserves the discrete total energy exactly.*

*Proof.* The change in kinetic (KE) and internal (IE) energy can be expressed as

$$\begin{aligned}KE^{n+1} - KE^n &= (\mathbf{v}^{n+1} - \mathbf{v}^n) \cdot \mathbf{M}_V \cdot \bar{\mathbf{v}}^{n+\frac{1}{2}} = -\Delta t (\mathbf{F}^{n+\frac{1}{2}} \cdot \mathbf{1}) \cdot \bar{\mathbf{v}}^{n+\frac{1}{2}} \\ IE^{n+1} - IE^n &= \mathbf{1} \cdot \mathbf{M}_E \cdot (\mathbf{e}^{n+1} - \mathbf{e}^n) = \Delta t \mathbf{1} \cdot (\mathbf{F}^{n+\frac{1}{2}})^T \cdot \bar{\mathbf{v}}^{n+\frac{1}{2}}.\end{aligned}$$

Therefore the discrete total energy is preserved:  $KE^{n+1} + IE^{n+1} = KE^n + IE^n$ .  $\square$

**7.2. Automatic time-step control.** To facilitate automatic time-step control, we define a time-step estimate  $\tau^n$  as the minimum (over all quadrature points used in the evaluation of the local force matrices  $\mathbf{F}_z$ ) of the expression:

$$\tau^n = \min_x \alpha \left( \frac{c_s(x)}{h_{\min}(x)} + \alpha_\mu \frac{\mu_s(x)}{\rho(x) h_{\min}^2(x)} \right)^{-1},$$

where  $h_{\min}(x)$  is the minimal singular value of  $\mathbf{J}_z(\hat{x})$  (divided by the kinematic space degree for high-order methods) and  $\alpha, \alpha_\mu$  are given ‘‘CFL’’ constants, which typically we define as  $\alpha = 0.5$  and  $\alpha_\mu = 2.5$ . In multistage time-stepping methods,  $\tau^n$  is taken to be the minimum over all stages. With this definition of  $\tau^n$ , we use the following algorithm to control the time-step:

1. Given a time-step  $\Delta t$  and state  $Y^n$ , evaluate the state  $Y^{n+1}$  and the corresponding time-step estimate  $\tau^n$ .
2. If  $\Delta t \geq \tau^n$ , set  $\Delta t = \beta_1 \Delta t$  and go to step 1.
3. If  $\Delta t \leq \gamma \tau^n$ , set  $\Delta t = \beta_2 \Delta t$ .
4. Set  $n = n + 1$  and continue with the next time-step.

Here,  $\beta_1, \beta_2$ , and  $\gamma$  denote given constants. The default values we use are  $\beta_1 = 0.85$ ,  $\beta_2 = 1.02$ , and  $\gamma = 0.8$ .

**8. Numerical Results.** We now present a series of numerical results using a set of high-order methods corresponding to specific choices for the finite element spaces describing the Lagrangian mesh coordinates  $x$ , the velocity  $v$  and the thermodynamic variable  $e$ . We consider several different test problems in both one, two and three space

dimensions, each designed to exercise and verify a particular aspect of Lagrangian hydrodynamics and of our high-order discretization methods. We begin by considering a set of "smooth" problems (i.e. problems without shock waves) to demonstrate some particular advantages of high-order curvilinear methods in this context. Next, we consider more complex shock wave test problems and demonstrate the advantages that high order methods can have in this context as well. For all test cases considered, we solve the global linear system for momentum conservation using a diagonally scaled conjugate gradient algorithm to a residual tolerance of  $10^{-8}$  and unless otherwise specified, we use an ideal gas equation of state with a constant adiabatic index  $\gamma = 5/3$ . For the shock wave test problems, we use the same set of artificial viscosity coefficients, namely  $q_1 = 1/2$  and  $q_2 = 2$ .

The results in this section have been computed in our high-order finite element Lagrangian hydrocode BLAST [39], which is based on the parallel modular finite element methods library MFEM [40]. We also used the related OpenGL visualization tool GLVis [41] to plot the computed curvilinear meshes and high-order fields.

**8.1. Taylor-Green 2D Vortex.** The purpose of this example is to verify the ability of our fully discrete methods to obtain high-order convergence in time and space on a moving mesh with non-trivial deformation for the case of a smooth (shock-free) problem. Here we consider a simple, steady state solution to the 2D incompressible, inviscid Navier Stokes equations, given by the the following velocity and pressure fields

$$\begin{aligned} v &= \{\sin(\pi x) \cos(\pi y), -\cos(\pi x) \sin(\pi y)\} \\ p &= \frac{\rho_0}{4}(\cos(2\pi x) + \cos(2\pi y)) \end{aligned}$$

We can extend this incompressible solution to the compressible case with an ideal gas equation of state and constant adiabatic index  $\gamma$ , by using a method of manufactured solution, meaning that we assume these initial conditions are steady state solutions to the Euler equations, then we solve for the resulting source terms and use these to drive the time dependent simulation. Applying this procedure, we arrive at an internal energy source term of the form

$$e = \frac{(\cos(2\pi x) + \cos(2\pi y))/4 + 1}{(\gamma - 1)\rho_0}$$

This procedure allows us to run the time dependent problem to some point in time then perform normed error analysis on the final computational mesh using the exact solutions for  $v$  and  $p$ . The computational domain is a unit box with wall boundary conditions on all surfaces ( $v \cdot \hat{n} = 0$ ). Since the initial conditions are also steady state solutions to the compressible equations (using the energy source mentioned above), these fields should remain constant for all time as the mesh moves in a Lagrangian manner. We run the problem to  $t = 0.75$ . Since this problem is smooth we run without any artificial viscosity, and do normed error analysis on the solution at the final time and compute convergence rates using a variety of high-order methods.

In Figure 8.1 we show plots of the (curvilinear) mesh and velocity field magnitude at times  $t = 0$  and  $t = 0.75$  using three different mesh / method combinations. The first case we consider is a  $Q_2$ - $Q_1$  method on an initially structured quadrilateral mesh using the energy conserving 2nd order RK2-Average time integration method (RK2Avg) presented in Section 7, the second case is a  $P_3$ - $P_2$  method on a triangular mesh (obtained by subdividing each zone of the previous quadrilateral mesh along

its diagonal) using a 3rd order strong stability preserving time integration method (RK3SSP) [42] while the final case is a  $Q_4$ - $Q_3$  method on an initially unstructured quadrilateral mesh using a 4th order time integration method (RK4). Note the degree to which each mesh is distorted as well as the curvilinear element boundaries in each case. In Figure 8.2 we plot error convergence (using the  $L_2$  norm) of the velocity magnitude at the final time  $t = 0.75$  for each case considered, on a sequence of four successively refined meshes. Note that for each case we observe the expected (high-order) convergence rates of 2nd, 3rd and 4th order, even on the highly deformed curvilinear mesh.

**8.2. 2D Single Material, Single-Mode Rayleigh-Taylor Instability.** The purpose of this example is to demonstrate the ability of high-order curvilinear methods to better resolve complex flow features and achieve greater robustness in a moving Lagrangian mesh when compared to mesh refined low order methods (with the same number of degrees of freedom). Here we consider a variation of the classic Rayleigh-Taylor instability problem [?] which consists of a heavy fluid resting on top of a light fluid in a gravitational field supported by a counterbalancing pressure gradient. The problem domain considered is  $(x, y) \in [0, L/2] \times [-L, L]$  with symmetry planes at  $x = 0$  and  $x = L/2$ , where  $L = 1$ . Initially, we have

$$\frac{dp}{dy} = \rho g$$

with  $p(y = L) = 2$  and the "gravitational" constant  $g = -1$ . For this problem, a purely Lagrangian method precludes the use of a two material state separated by a contact discontinuity since the flow will form a "slide" surface with discontinuous velocities at the interface. We therefore consider the case of a single material with an initial smooth density gradient in the vertical (or  $y$ ) direction given by

$$\rho(y) = \frac{(\rho_1 + \rho_2)}{2} + \frac{(\rho_2 - \rho_1)}{\arctan(\beta y)}$$

where  $\rho_1 = 1$  which represents the "light" material,  $\rho_2 = 2$  which represents the "heavy" material and the smoothing parameter  $\beta = 20$ . To set up the hydrodynamic instability across the initial density gradient, we apply an initial velocity perturbation of wavelength  $L$  to the whole problem given by

$$v = v_0 \{2y \exp(-2\pi y^2) \sin(2\pi x), \exp(-2\pi y^2) \cos(2\pi x)\}$$

As with the previous problem, this problem is smooth and we therefore run without any artificial viscosity.

In Figure 8.3 we show plots of the (curvilinear) mesh and density field at different snapshots in time corresponding to  $t = 3.0$ ,  $t = 4.0$ ,  $t = 4.5$  and  $t = 5.0$  for the case of four different high-order curvilinear methods:  $Q_1$ - $Q_0$  (analogous to traditional SGH),  $Q_2$ - $Q_1$ ,  $Q_4$ - $Q_3$  and  $Q_8$ - $Q_7$ . In each case, the total number of kinematic and thermodynamic degrees of freedom is held constant. This is achieved by de-refining the mesh one level for every doubling of the spatial order of the method used. Note that as time increases and the problem develops more vorticity, the low order methods begin to "lock-up" and are no longer able to resolve the flow as the mesh begins to tangle. As the order of the method is increased, the problem is able to run further in time and resolve more of the flow features while maintaining robustness in the Lagrangian mesh.



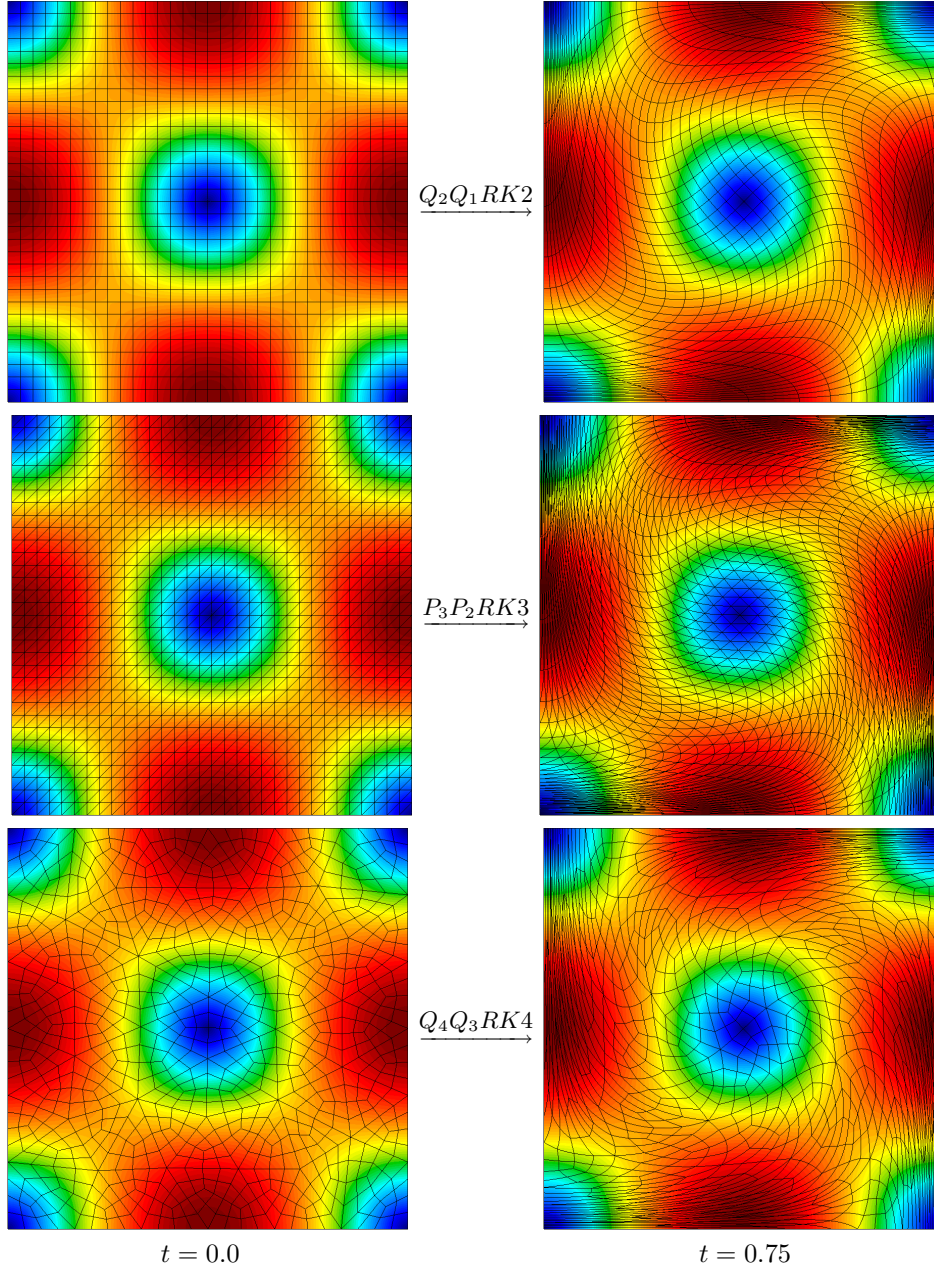


FIG. 8.1. Initial ( $t = 0.0$ ) and final ( $t = 0.75$ ) curvilinear mesh and velocity field magnitudes for the 2D Taylor-Green vortex problem using three different combinations of meshes and high-order methods.

**8.3. Sod Shock Tube.** We now transition to shock wave problems which require the use of artificial viscosity for shock capturing. The purpose of this example is to verify the ability of our high-order methods to propagate shocks, rarefaction waves and contact discontinuities in 1D. We consider a simple 1D Riemann problem, the Sod shock tube, on the domain  $x \in [0, 1]$  consisting of two materials with different

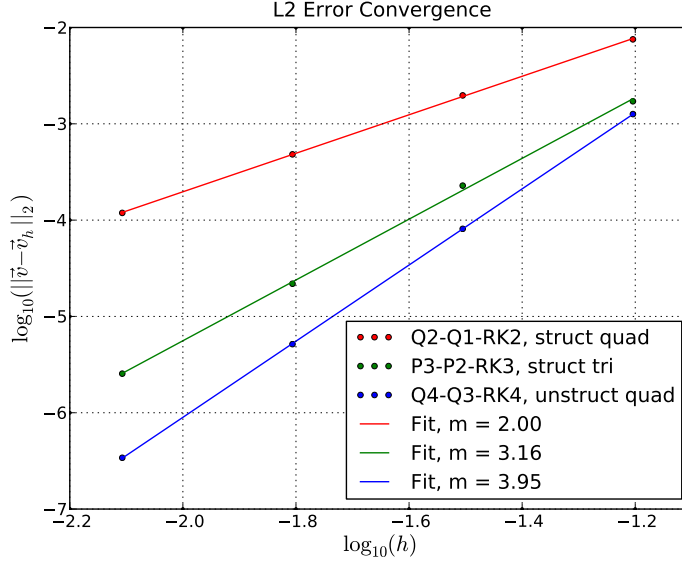


FIG. 8.2. Error convergence in velocity magnitude using the  $L_2$  norm for the 2D Taylor-Green vortex problem using three different combinations of meshes and high-order methods.

initial states denoted L (left) and R (right), separated by a contact discontinuity at  $x = 0.5$ . Results on this benchmark using a  $Q2-Q1$  method have been reported in [36], here we compare the same problem using a  $Q8-Q7$  method with an identical number of degrees of freedom. The initial conditions are given by

$$\begin{aligned} v_L &= \{0, 0\}, \quad \rho_L = 1, \quad e_L = \frac{3}{2} \\ v_R &= \{0, 0\}, \quad \rho_R = \frac{1}{8}, \quad e_R = \frac{6}{5} \end{aligned}$$

Since the problem is 1D, it eliminates multi-dimensional discretization issues and focuses on the shock capturing properties of our high-order methods such as diffusion and Gibb's like ringing at shock fronts as well as possible (non-physical) shock entropy production in rarefaction waves.

In Figure 8.4 we show scatter plots of the velocity, density, internal energy and pressure vs. the  $x$ -coordinate at the final time of  $t = 0.2$  and compare to the analytic solution using both a  $Q8-Q7$  method on a "1D" 50 zone mesh (consisting of 50 zones in the  $x$  direction and a single zone in the  $y$  direction with  $y \in [0, 0.1]$ ) and a  $Q2-Q1$  method on a twice refined version of the same mesh (i.e. each zone is subdivided twice in each dimension, resulting in 200 zones in the  $x$  direction and 4 zones in the  $y$  direction, again with  $y \in [0, 0.1]$ ). For each plot, the fields are sampled using the underlying high order finite element basis function representation with 25 plot points per zone (5 in the  $x$ -direction) for the  $Q2-Q1$  method and 400 plot points per zone (20 in the  $x$ -direction) for the  $Q8-Q7$ . The sampling of the solutions at the sub-zone level is essential to resolve the high-order data that is present in the solution. In both cases we capture the material contact discontinuity without any diffusion (since we are using a discontinuous internal energy basis), and in both cases we observe the "wall heating" phenomenon in the internal energy and its subsequent effect on the

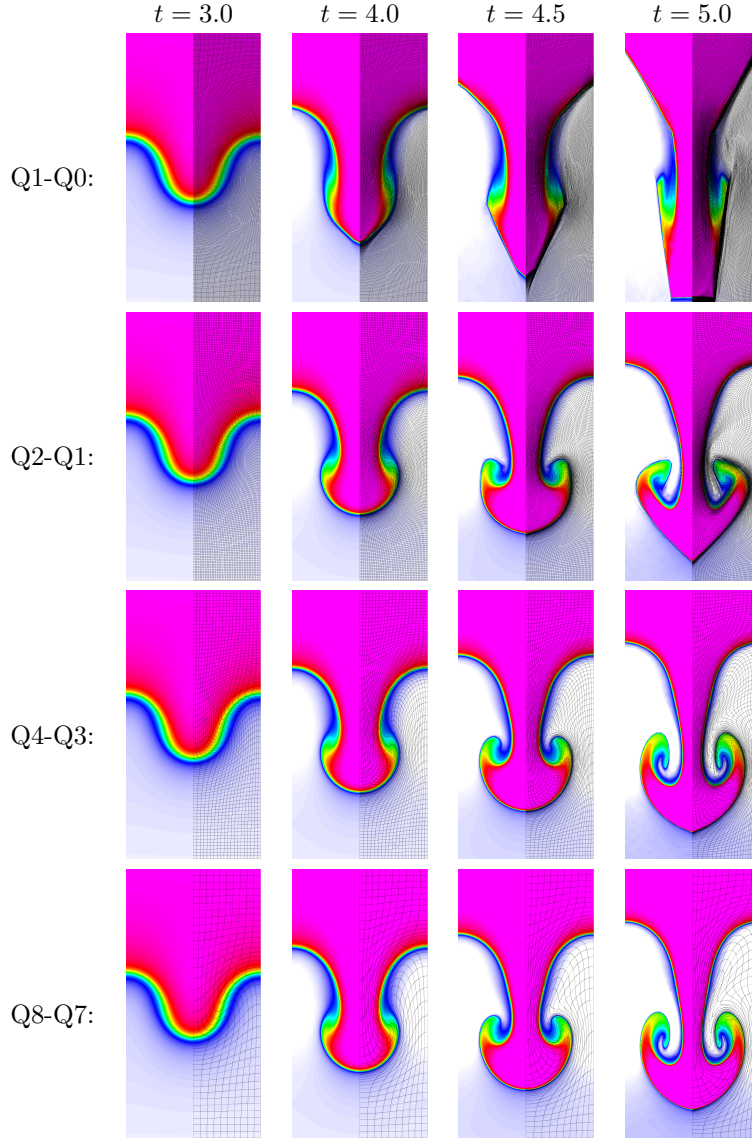


FIG. 8.3. Snapshots in time corresponding to  $t = 3.0$ ,  $t = 4.0$ ,  $t = 4.5$  and  $t = 5.0$  for the single material, single-mode Rayleigh-Taylor instability problem using a sequence of high-order methods with a fixed number of degrees of freedom for each case.

density at the contact. Furthermore, we can conclude for both cases that the ability to resolve the rarefaction wave is evidence that our artificial viscosity is not excessively damping the solution in smooth regions. Note that the low order method on the fine mesh yields essentially the same result as the high-order method on the coarse mesh.

In Figure 8.5 we show plots of the velocity and density zoomed in around the shock front. In addition, we designate with color-coded vertical lines the zone boundary around the shock for the  $Q8-Q7$  method and the corresponding four refined zones for the  $Q2-Q1$ . Here we can more clearly see the high-order, sub-zonal variation in both the continuous velocity and piecewise discontinuous density. For the  $Q8-Q7$ , the shock

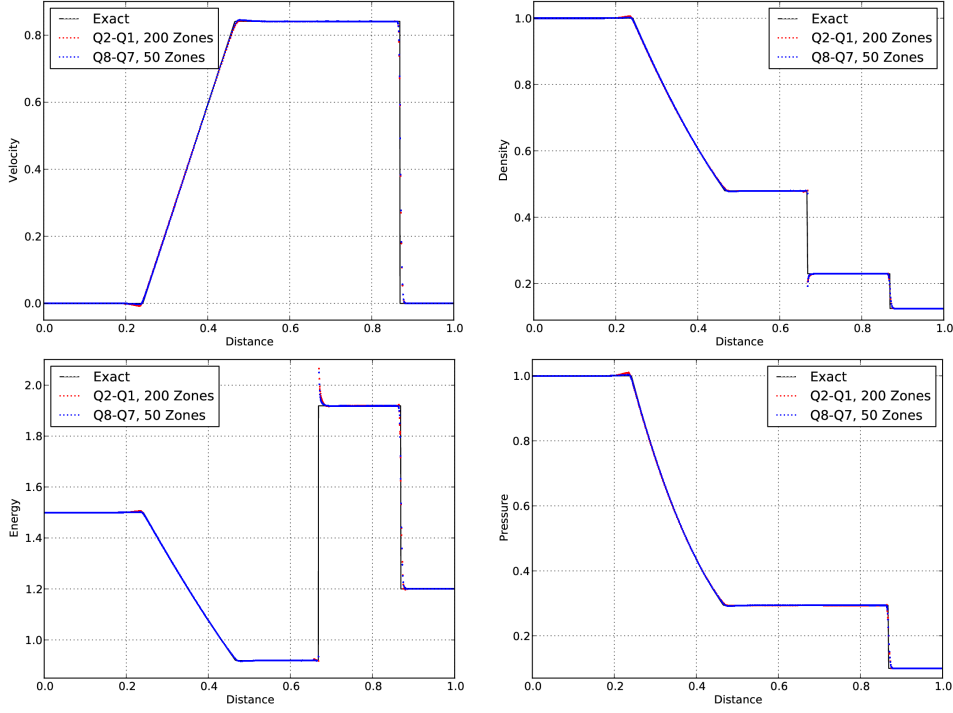


FIG. 8.4. Results for the Sod shock tube on a 200 zone mesh using a  $Q2-Q1$  method and a 50 zone mesh using a  $Q8-Q7$  method: velocity (top-left), density (top-right), internal energy (bottom-left) and pressure (bottom-right),

is entirely resolved in a single zone. Note that even though we using an 8th order polynomial basis for the velocity and a 7th order polynomial basis for the internal energy for  $Q8-Q7$  method, we do not observe spurious oscillations at the shock front.

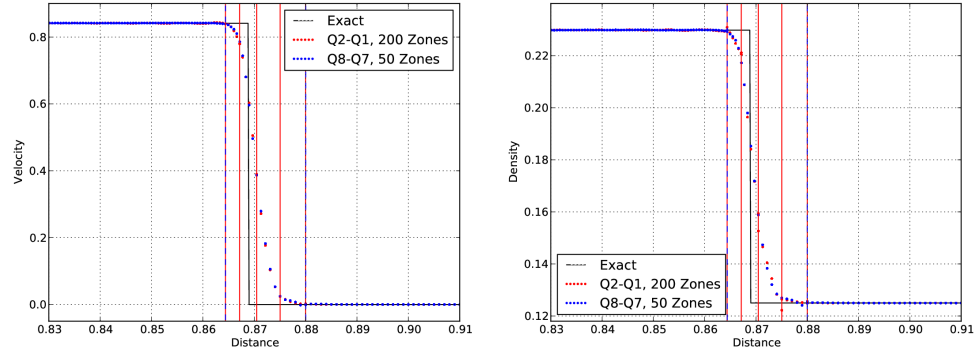


FIG. 8.5. Results for the Sod shock tube on a 200 zone mesh using a  $Q2-Q1$  method and a 50 zone mesh using a  $Q8-Q7$  method: zoomed in around the shock front illustrating the high-order continuous velocity (left) and discontinuous density (right). The zone boundaries around the shock are designated with color-coded vertical lines.

**8.4. Sedov Explosion and Noh Implosion on Distorted Grids.** The purpose of these examples is to demonstrate the benefits of our high-order artificial vis-

cosity formulation in maintaining symmetry for shock wave propagation over irregular meshes. Here we consider both the Sedov explosion [43] and the Noh implosion [44] test problems in planar  $x$ - $y$  geometry. The Sedov problem consists of an ideal gas ( $\gamma = 1.4$ ) with a delta function source of internal energy deposited at the origin such that the total integrated energy  $E_{tot} = 1$ . The sudden release of the energy creates an expanding shock wave, converting the initial internal energy into kinetic energy. The delta function energy source is approximated by setting the internal energy  $e$  to zero in all degrees of freedom except at the origin where the value is chosen so that the total internal energy is 1. The Noh problem consists of an ideal gas with  $\gamma = 5/3$ , initial density  $\rho_0 = 1$  and initial energy  $e_0 = 0$ . The value of each  $Q_2$  velocity degree of freedom is initialized to a radial vector pointing toward the origin,  $v = -\vec{r}/\|\vec{r}\|$ . The initial velocity generates a stagnation shock wave that propagates radially outward and produces a peak post-shock density of  $\rho = 16$ .

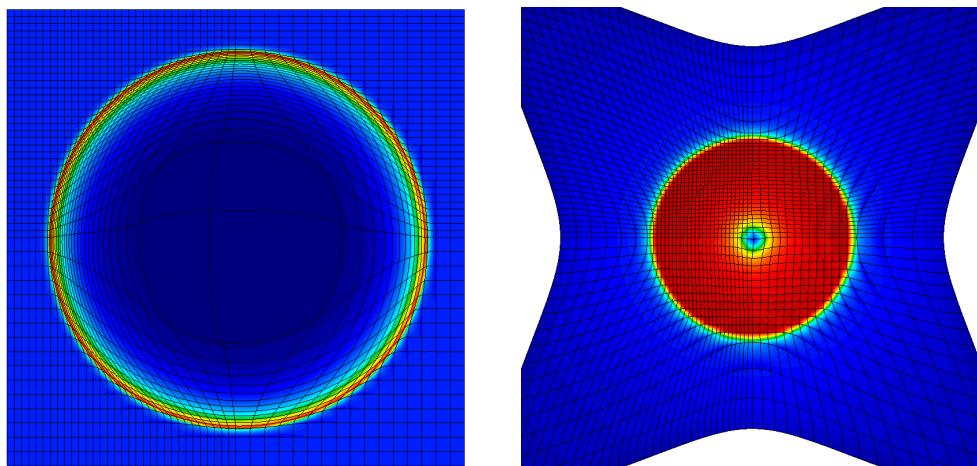


FIG. 8.6. Density field and curvilinear mesh for the Sedov problem (left) and the Noh problem (right) on a Cartesian grid with different mesh spacing in different quadrants.

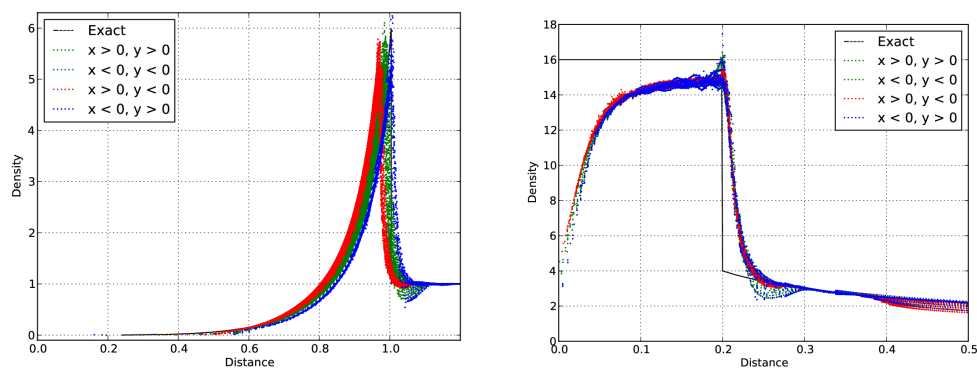


FIG. 8.7. Scatter plots of density vs. radius, colored by quadrant, for the Sedov problem (left) and the Noh problem (right) on a Cartesian grid with different mesh spacing in different quadrants.

**8.5. 2D Multi-Material Shock Triple Point Interaction.** The purpose of this example is to demonstrate that the results from Section 8.2 carry over to multi-



material shock driven problems as well. Here we consider a three state, two material, 2D Riemann problem which generates vorticity. The problem domain and initial conditions are depicted in Figure 8.8. This problem tests the ability of our methods to propagate shock waves over multi-material regions and handle complex mesh motion due to vorticity. For a Lagrangian method, there is a limit to how long this problem can be run due to the generation of vorticity. Here we demonstrate the superior advantage that high-order curvilinear methods can provide in this context.

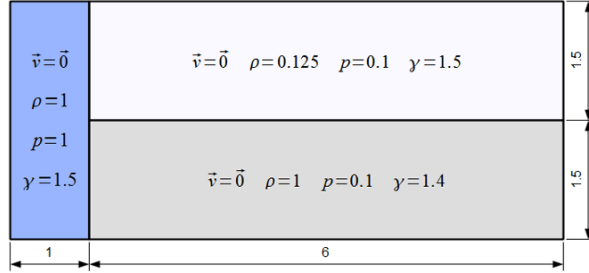


FIG. 8.8. Initial conditions for the 2D multi-material shock triple point interaction problem.

In Figure 8.9 we show plots of the (curvilinear) mesh and density field (log scale) at different snapshots in time corresponding to  $t = 3.0$  and  $t = 5.0$  for the case of three different high-order curvilinear methods:  $Q_2$ - $Q_1$ ,  $Q_4$ - $Q_3$  and  $Q_8$ - $Q_7$ . In each case, the total number of kinematic and thermodynamic degrees of freedom is held constant. This is achieved by de-refining the mesh one level for every doubling of the spatial order of the method used.

**8.6. 3D Multi-Material Spherical Implosion.** The purpose of this example is to demonstrate the benefits of high-order curvilinear methods with respect to symmetry preservation in 3D problems. Maintaining spherical symmetry on 3D unstructured meshes remains a major challenge for most Lagrangian (or ALE) schemes. Here we consider a simple 1D multi-material implosion problem on an unstructured 3D mesh. The problem consists of a low density material with  $\rho_1 = 0.05$  in the radial range  $r \in [0, 1]$  surrounded by a shell of high density material  $\rho_2 = 1.0$  in the radial range  $r \in [1.0, 1.2]$ . Each material is at an initial pressure of  $p = 0.1$  and uses an ideal gas equation of state with  $\gamma = 5/3$ . This problem was originally proposed by [45] for cylindrical symmetry. Here we make a simple modification for spherical symmetry, instead of applying a time dependent pressure source to the outermost radial surface of the problem, we apply a constant velocity source of  $v = -5\vec{r}/\|\vec{r}\|$ .

The outer surface drives a spherical shock wave inward. Ideally, the interface between the high and low density materials should remain perfectly spherical for all time due to the spherical symmetry of the velocity drive. However, the discretization errors of the initial geometry of this surface and subsequent error introduced by the numerical algorithm will be amplified over time since the interface is subject to both Richtmyer-Meshkov (RM) and Rayleigh-Taylor (RT) instabilities. In Figure 8.10 we show plots of the mesh and density at three snapshots in time using a  $Q_1$ - $Q_0$  method. In Figure 8.11 we show the same plots using a high order  $Q_2$ - $Q_1$  method on a curvilinear mesh that is de-refined one level so that the two cases have an identical number of kinematic and thermodynamics degrees of freedom. In Figure 8.12 we plot the average radius of the entire material interface (surface) sampled at 9 points per

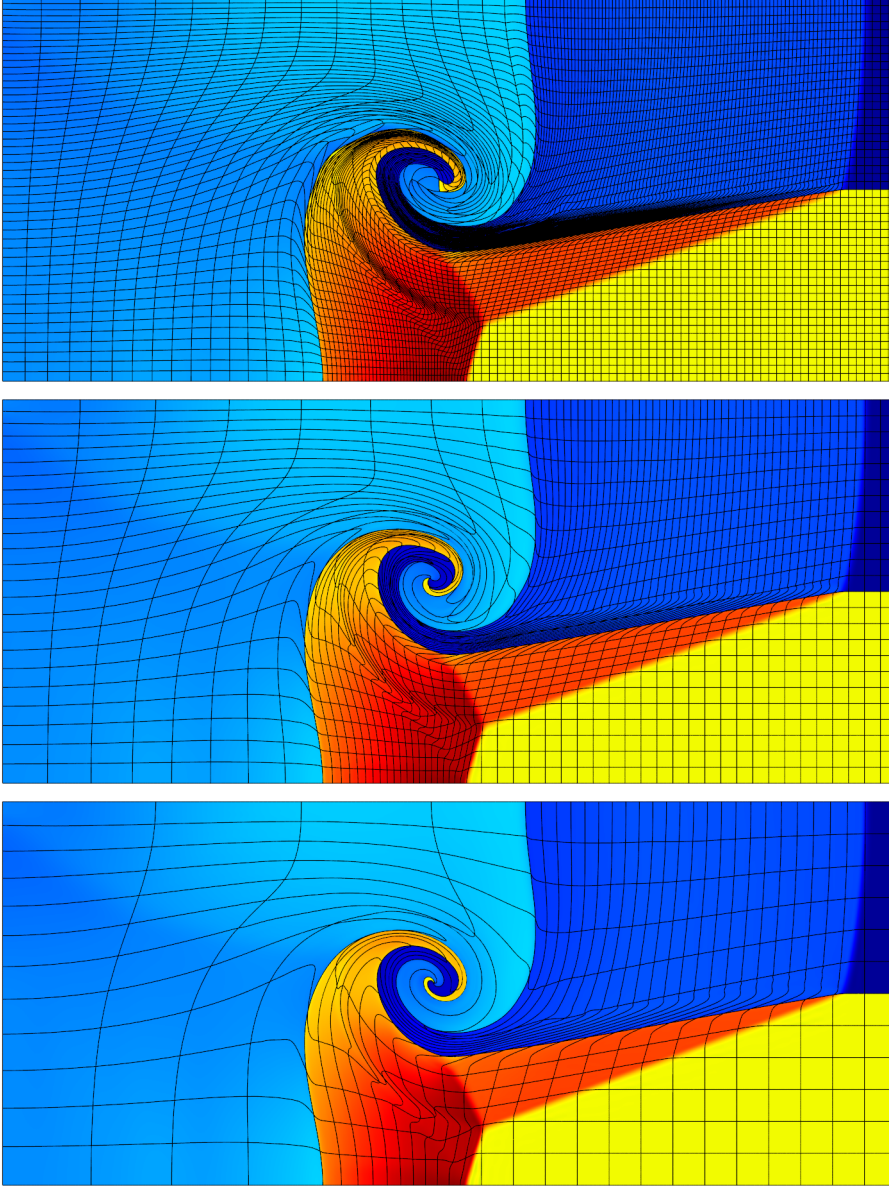


FIG. 8.9. Results for density (log scale) and curvilinear mesh in the shock triple point problem at time  $t = 3.0$  using a sequence of high order methods with a fixed number of degrees of freedom for each case.

face for the  $Q1-Q0$  method and 25 points per face for  $Q2-Q1$  and compare this to reference 1D result (obtained from a high resolution 1D Lagrangian SGH calculation). Note that both methods achieve essentially the same results in the average radius. In Figure 8.12 we also plot the normalized standard deviation of this radial surface which indicates the symmetry error over time. Note that  $Q2-Q1$  method is much better at preserving both the initial and time evolved symmetry of the interface for a fixed number of degrees of freedom. This is demonstrated further in Figure 8.13 where we

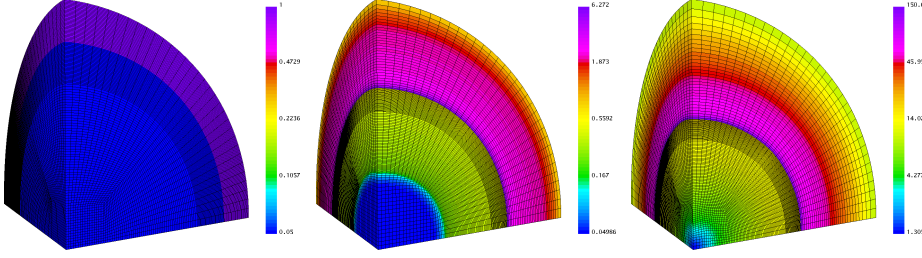


FIG. 8.10. Snapshots of mesh and density (log scale) at times  $t = 0$ ,  $t = 0.081$  and  $t = 0.18$  for the 3D multi-material spherical implosion problem using a Q1-Q0 method.

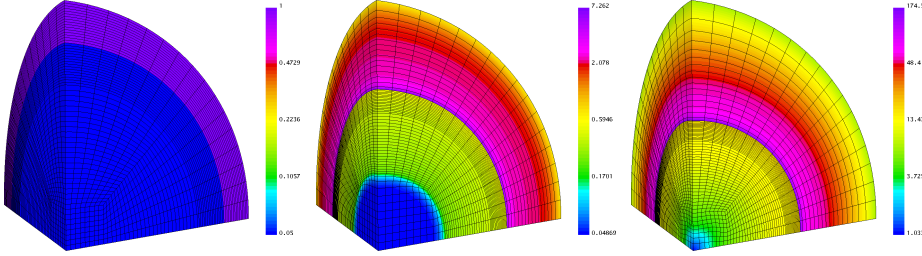


FIG. 8.11. Snapshots of mesh and density (log scale) at times  $t = 0$ ,  $t = 0.081$  and  $t = 0.18$  for the 3D multi-material spherical implosion problem using a Q2-Q1 method.

plot of the calculate radius at the final time of  $t = 0.18$  for both cases.

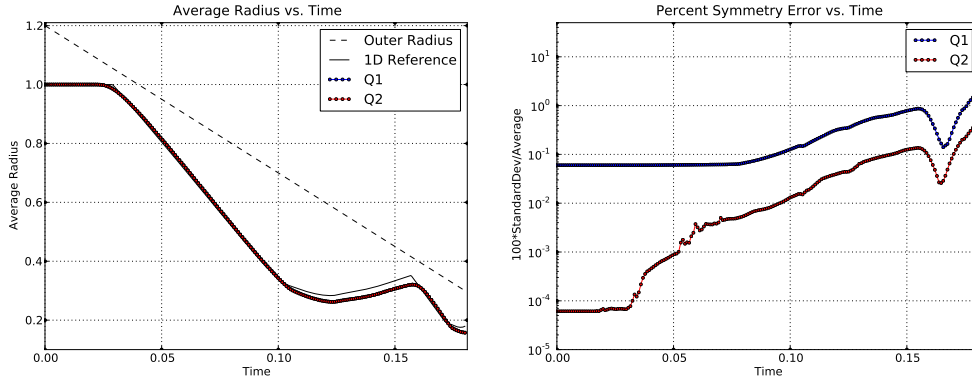


FIG. 8.12. Average interface radius vs. time and percent symmetry error vs. time.

**9. Conclusions.** We have developed and presented a general high order curvilinear finite element approach for solving the equations of compressible hydrodynamics in a Lagrangian frame. This approach is general with respect to the choice of kinematic and thermodynamic basis and we shown that under simplifying low order assumptions, we can exactly recover classical methods. We have demonstrated via numerical examples the benefits that can be obtained by using high order curvilinear methods including the ability to more accurately capture geometrical features of a flow region and maintain robustness with respect to mesh motion using curvilinear zones, significant improvements in symmetry preservation for symmetric flows, elimination of



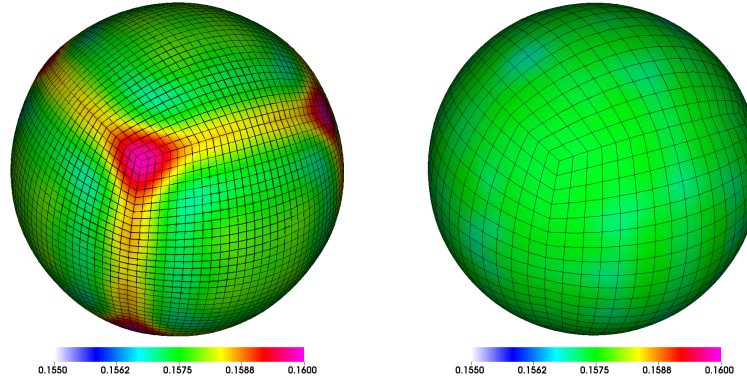


FIG. 8.13. Plots of interface radius using a fixed color scale for the 3D multi-material spherical implosion problem at time  $t = 0.18$  using both a  $Q1$ - $Q0$  method (left) and a  $Q2$ - $Q1$  method (right).

the need for ad-hoc hourglass filters, sharper resolution of a shock front for a given mesh resolution including the ability to represent a shock within a single zone and a substantial reduction in mesh imprinting for shock wave propagation not aligned with the computational mesh.

#### REFERENCES

- [1] D. J. Benson. Computational methods in Lagrangian and Eulerian hydrocodes. *Comput. Methods Appl. Mech. Engrg.*, 99:235–394, 1992.
- [2] M. L. Wilkins. *Methods in Computational Physics*, volume 3, chapter Calculation of Elastic-Plastic Flow. Academic Press, 1964.
- [3] R. Tipton. CALE Lagrange step. Technical report, Lawrence Livermore National Laboratory, October 1990. Unpublished.
- [4] R. Tipton. Hourglass modes and a new monotonic hourglass filter. Technical report, Lawrence Livermore National Laboratory, December 1999. Unpublished.
- [5] J. VonNeumann and R. D. Richtmyer. A method for the numerical calculation of hydrodynamic shocks. *J. Appl. Phys.*, 21:232–237, 1950.
- [6] B. Depres and C. Mazeran. Lagrangian gas dynamics in two dimensions and Lagrangian systems. *Arch. Rational Mech. Anal.*, 178(3):327–372, 2005.
- [7] P-H. Maire, R. Abgrall, and P. Vachal. Staggered Lagrangian discretization based on cell-centered Riemann solver and associated hydrodynamics scheme. *SIAM J. Sci. Comp.*, 29(4):1781–1824, 2007.
- [8] P-H. Maire. A high-order cell-centered Lagrangian scheme for two-dimensional compressible fluid flows on unstructured meshes. *J. Comput. Phys.*, 228(7):2391–2425, 2009.
- [9] R. B. Christensen. Godunov methods on a staggered mesh – An improved artificial viscosity. Technical Report UCRL-JC-105269, Lawrence Livermore National Laboratory, 1991.
- [10] P-H. Maire, R. Loubere, and P. Vachal. Staggered Lagrangian discretization based on cell-centered Riemann solver and associated hydrodynamics scheme. *Commun. Comput. Phys.*, 10:940–978, 2011.
- [11] J. K. Dukowicz and B. J. Meltz. Vorticity errors in multidimensional lagrangian codes. *J. Comput. Phys.*, 99(1):115–134, 1992.
- [12] C. W. Hirt, A. A. Amsden, and J. L. Cook. An arbitrary Lagrangian-Eulerian computing method for all flow speeds. *J. Comput. Phys.*, 14:277–253, 1974.
- [13] D. J. Benson. An efficient, accurate, and simple ALE method for nonlinear finite element programs. *Comput. Methods Appl. Mech. Engrg.*, 72:305–350, 1989.
- [14] P. Kjellgren and J. Hyvarien. An arbitrary Lagrangian-Eulerian finite element method. *Comp. Mech.*, 21:81–90, 1998.
- [15] R. M. Darlington, T. L. McAbee, and G. Rodrigue. A study of ALE simulations of Rayleigh-Taylor instability. *Comp. Phys. Comm.*, 135(1):58–73, 2001.
- [16] D. E. Burton. Multidimensional discretizations of conservation laws for unstructured polyhedral

- grids. Technical Report UCRL-JC-118306, Lawrence Livermore National Laboratory, 1994.
- [17] E. J. Caramana, D. E. Burton, M. J. Shashkov, and P. P. Whalen. The construction of compatible hydrodynamics algorithms utilizing conservation of total energy. *J. Comput. Phys.*, 146:227–262, 1998.
  - [18] E. J. Caramana and M. J. Shashkov. Elimination of artificial grid distortion and hourglass-type motions by means of Lagrangian subzonal masses and pressures. *J. Comput. Phys.*, 142(2):521–561, 1998.
  - [19] E. J. Caramana, M. J. Shashkov, and P. P. Whalen. Formulations of artificial viscosity for multi-dimensional shock wave computations. *J. Comput. Phys.*, 144:70–97, 1998.
  - [20] J. C. Campbell and M. J. Shashkov. A tensor artificial viscosity using a mimetic finite difference algorithm. *J. Comput. Phys.*, 172:739–765, 2001.
  - [21] J. C. Campbell, J. M. Hyman, and M. Shashkov. Mimetic finite difference operators for second-order tensors on unstructured grids. *Comput. Math. Appl.*, 44:157–173, 2002.
  - [22] Tz. V. Kolev and R. N. Rieben. A tensor artificial viscosity using a finite element approach. *J. Comput. Phys.*, 228(22):8336–8366, 2009.
  - [23] G. Scovazzi. Stabilized shock hydrodynamics: II. Design and physical interpretation of the SUPG operator for Lagrangian computations. *Comput. Methods Appl. Mech. Engrg.*, 196:966–978, 2007.
  - [24] G. Scovazzi, E. Love, and M. Shashkov. Multi-scale Lagrangian shock hydrodynamics on Q1/P0 finite elements: Theoretical framework and two-dimensional computations. *Comput. Methods Appl. Mech. Engrg.*, 197:1056–1079, 2008.
  - [25] A. Barlow. A compatible finite element multi-material ALE hydrodynamics algorithm. *Internat. J. Numer. Methods Fluids*, 56:953–964, 2007.
  - [26] P. G. Ciarlet. *The Finite Element Method for Elliptic Problems*. North-Holland, 1978.
  - [27] R. Rieben, D. White, and G. Rodrigue. A high order mixed vector finite element method for solving the time dependent Maxwell equations on unstructured grids. *J. Comput. Phys.*, 204:490–519, 2005.
  - [28] P. Castillo, R. Rieben, and D. White. FEMSTER: An object oriented class library of higher-order discrete differential forms. *ACM Trans. Math. Soft.*, 31(4):425–457, 2005.
  - [29] R. Rieben and D. White. Verification of high-order mixed FEM solution of transient magnetic diffusion problems. *IEEE Trans. Mag.*, 42(1):25–39, 2006.
  - [30] P. Bochev. *Least-squares finite element methods for the Stokes and Navier-Stokes equations*. PhD thesis, Virginia Polytechnic Institute and State University, Blacksburg, Virginia, 1994.
  - [31] R. N. Rieben, D. A. White, B. K. Wallin, and J. M. Solberg. An arbitrary Lagrangian-Eulerian discretization of MHD on 3D unstructured grids. *J. Comput. Phys.*, 226:534–570, 2007.
  - [32] L. Margolin and M. Shashkov. Using a curvilinear grid to construct symmetry-preserving discretizations for Lagrangian gas dynamics. *J. Comput. Phys.*, 149:389–417, 1999.
  - [33] H. Ockendon and J. Ockendon. *Waves and Compressible Flow*, volume 47 of *Texts in Applied Mathematics*. Springer-Verlag, 2004.
  - [34] J. Felcman, M. Feistauer, and I. Straškraba. *Mathematical and Computational Methods for Compressible Flow*. Clarendon Press, Oxford, 2003.
  - [35] F. H. Harlow and A. A. Amsden. Fluid dynamics: A LASL monograph. Technical Report LA-4700, Los Alamos Scientific Laboratory, 1971.
  - [36] V. A. Dobrev, T. E. Ellis, Tz. V. Kolev, and R. N. Rieben. Curvilinear finite elements for Lagrangian hydrodynamics. *Internat. J. Numer. Methods Fluids*, 65(11-12):1295–1310, 2010.
  - [37] B. VanLeer. Towards the ultimate conservative difference scheme. *J. Comput. Phys.*, 32(1):101–136, 1979.
  - [38] R. Landshoff. A numerical method for treating fluid flow in the presence of shocks. Technical Report LA-1930, Los Alamos National Laboratory, 1955.
  - [39] BLAST: a high-order finite element Lagrangian hydrocode. <http://www.llnl.gov/CASC/blast>.
  - [40] MFEM: a modular finite element methods library. <http://mfem.googlecode.com>.
  - [41] GLVis: an OpenGL visualization tool. <http://glvis.googlecode.com>.
  - [42] S. Gottlieb, C. Shu, and E. Tadmor. Strong stability preserving high order time discretization methods. *SIAM Rev.*, 43:89–112, 2001.
  - [43] L. I. Sedov. *Similarity and Dimensional Methods in Mechanics*. CRC Press, tenth edition, 1993.
  - [44] W. F. Noh. Errors for calculations of strong shocks using an artificial viscosity and an artificial heat flux. *J. Comput. Phys.*, 72(1):78–120, 1987.
  - [45] S. Galera, P.-H. Maire, and J. Breil. A two-dimensional unstructured cell-centered multi-material ALE scheme using VOF interface reconstruction. *J. Comput. Phys.*, 229(16):5755–5787, 2010.